doi.org/10.1016/j.ijggc.2018.01.004

Numerical Analysis of Mixed-Mode Rupture Propagation of Faults in Reservoir-Caprock System in CO_2 Storage

Sohrab Gheibi [a*], Victor Vilarrasa [b, c], Rune M. Holt [a]

[a] Department of Geoscience and Petroleum, Norwegian University of Science and Technology (NTNU), S. P. Andersens veg 15a, 7031 Trondheim, Norway

[b] Institute of Environmental Assessment and Water Research (IDAEA), Spanish National Research Council (CSIC), Jordi Girona 18-26, 08034 Barcelona, Spain

[c] Associated Unit: Hydrogeology Group (UPC-CSIC), Spain

Abstract

Injection-induced seismicity and caprock integrity are among the most important concerns in CO_2 storage operations. Understanding and minimizing fault/fracture reactivation in the first place, and rupture growth/propagation beyond its surface afterwards, are fundamental to achieve a successful deployment of geologic carbon storage projects. Rock fracture mechanics provides useful concepts to study the propagation of discontinuities such as pre-existing faults and fractures. In this paper, we aim at developing a methodology to investigate the rupture propagation likelihood of faults/fractures inside a reservoir and its surrounding (including the caprock) as a result of reservoir pressurization. In this methodology, mode I (tensile) and mode II (shear) stress intensity factors of a given fault/fracture are calculated based on Linear Elastic Fracture Mechanics. A fault/fracture can propagate either in mode I, mode II or a combination of both (also called mixed-mode) based on the comparison of the stress intensity factors and fracture toughness. The proposed methodology, which has been embedded into a hybrid Finite Element Method-Discrete Element Method in-house code called MDEM, has the capability to obtain the direction of mode I and mode II rupture in front of a fault/fracture tip. Two coefficients are defined as stress intensity paths (κ) for a fault/fracture, as the change of stress intensity factors for the two failure modes of a given discontinuity per unit pore pressure change of the reservoir after injection. Based on these stress intensity path coefficients, a relationship is given to

doi.org/10.1016/j.ijggc.2018.01.004

calculate the threshold pressure buildup above which the two propagation modes may occur. We use the proposed methodology to investigate the rupture growth likelihood of faults in and around a closed reservoir due to its pressurization. Simulation results indicate that mode I failure is likely to occur inside the reservoir for faults with low dip angle in compressional stress regimes. However, the initiated mode I failure may not have the chance to grow upwards because the minimum principal is in the vertical direction and thus, the initiated rupture tends to rotate and grow horizontally. In contrast, mode I rupture is likely to occur in the caprock for faults with high dip angle in extensional stress regimes. The initiated rupture may grow upwards if the newly created fracture becomes hydraulically connected with the reservoir. We find that mode II rupture is not likely to occur in any of the investigated scenarios. Simulation results show that the coefficients of the stress intensity factors depend on the faults location, dipping angle, fault length, presence of other faults, reservoir aspect ratio and reservoir and caprock stiffness.

Keywords: Fault reactivation, stress intensity path, fracture propagation, caprock integrity, induced seismicity, CO_2 storage

* Corresponding author:
E-mail address: sohrabgheibie@gmail.com

doi.org/10.1016/j.ijggc.2018.01.004

1. Introduction

CO_2 storage is considered as one of the options to reduce carbon dioxide (CO_2) in the atmosphere to mitigate its effect on climate change. Safety of the injection from a geomechanical point of view has been a concern among scientists and the public. The main geomechanical risks associated with storage of CO_2 are differential ground displacement due to surface uplift, caprock integrity and fault reactivation leading to leakage and/or seismicity (Streit and Hillis, 2004; Rutqvist, 2012; White and Foxall, 2016).

Industrial scale injection of CO_2 in the subsurface will cause ground heave as a result of pore pressure increase (Rutqvist, 2012). A well-known example of this heave is the double-lobe uplift measured at In Salah, Algeria, on top of a horizontal injection well (Vasco et al., 2010). If uplift occurs over a large area and is relatively uniform, ground movement should not imply any problem. Actually, it has been proposed to inject CO_2 below Venice, Italy, in order to compensate for the subsidence that is sinking the city below the sea level (Comerlati et al., 2006). Nevertheless, structural problems may appear if differential uplift becomes significant. Apart from ground movement, another source of concern is CO_2 leakage that could be related to loss of caprock sealing capacity and/or fault stability. Given the characteristics of CO_2 pressure evolution, which becomes practically constant after a sharp initial increase, caprock integrity is unlikely to be compromised if proper pressure management is performed (Vilarrasa and Carrera, 2015). On the other hand, fault stability may be an issue because fault reactivation could give rise to both CO_2 leakage and felt induced seismicity that may raise public concern (Rinaldi et al., 2014; Rutqvist et al., 2016; Vilarrasa et al., 2016).

There are several geomechanical studies that explicitly include faults in CO_2 storage models investigating faults/fractures reactivation (e.g., Vidal-Gilbert et al., 2010; Cappa and Rutqvist, 2011; Rinaldi et al., 2015; Gheibi et al., 2016, 2017). These studies focus only on fault plane stability and exclude the effect of fault tip. In other words, they do not investigate the growth/propagation of reactivated faults. In particular, studies of fault/fracture stability from a fracture mechanics point of view are limited in CO_2 storage. This limitation is probably due to the fact that geomechanical studies related to CO_2 storage are relatively small in number and have focused on other types of problems.

One of the most challenging issues related to fault modeling is obtaining the stress values in front of the fault tip. On the one hand, based on elastic solutions, namely Linear Elastic Fracture Mechanics (LEFM), the stress value is singular at a crack/fault tip. Therefore, calculation of the stress values is mesh size dependent in numerical modeling. Actually, the calculated stress becomes greater for finer elements. Thus, a stress-strength failure criterion that use the stress state to evaluate whether the strength is reached cannot be adopted. This mesh size dependency can be avoided if an appropriate fracture mechanics criteria, such as energy release rate, g^c, or fracture toughness, K^C, is used. There are three types of rock fracture propagation, i.e., tensile opening, shearing and tearing modes, and their corresponding Stress Intensity Factors (SIF) are K^I, K^{II} and K^{III}, respectively (Bazant and Planas, 1997) . On the other hand, based on non-elastic solutions, no material can withstand the very high stress values in the crack/fault tip. As a result, stresses will drop to a limit due to material plasticity or softening in quasi-brittle materials. Examples of existing solutions are Cohesive Zone Modeling (Elice, 2002) and Crack Band Theory (Bazant and Oh, 1983).

Among the few studies related to CO_2 storage that consider fracture/fault propagation, Wang et al. (2016) developed an analytical method to calculate the change of SIF of a fault located in the caprock due to fluid injection and withdrawal. Nevertheless, their methodology is limited to mode II and cannot calculate the magnitude of the SIF. On the other hand, Papanastasiou et al. (2016) presented an analytical model of hydraulic fracturing in weak formations to investigate the risk of hydraulic fracturing in CO_2 storage. The analytical model of Papanastasiou et al. (2016), which is limited to mode I, is based on a Mohr–Coulomb dislocation model that is extended to account for materials with fracture toughness. They found that a hydraulically induced fracture from CO_2 injection is more likely to propagate horizontally than vertically, remaining contained in the storage formation.

The goal of this paper is to develop a methodology to calculate both mode I and mode II SIF of faults inside reservoir and caprock based on LEFM. The methodology has been implemented into a hybrid Finite Element Method (FEM)-Discrete Element Method (DEM) code called MDEM (Alassi, 2008; Lavrov et al., 2015). For reasonably fine meshed, a significant dependency of the solution on the mesh size is not observed. We also introduce stress intensity path coefficients as the change of SIF per unit

doi.org/10.1016/j.ijggc.2018.01.004

pore pressure change in the reservoir. We use the methodology to investigate the effect of several parameters, such as (i) fault length, (ii) inclination, (iii) location, (iv) elastic properties of reservoir and caprock and the contrast between them, (v) interaction of faults on each other and (vi) reservoir aspect ratio, on the stress intensity path. We also perform fault rupture analysis as a result of reservoir pressurization using the introduced stress intensity paths coefficients.

2. Methods

2.1 Mixed mode I-II cracks and brittle fracture criterion

Using the linear superposition of stresses in polar coordinates, the elastic state of stress around the crack tip is (after Lawn, 1975)

$$\sigma_{rr} = \frac{1}{2\sqrt{2\pi r}}\left[K^{I}\left(3-\cos\theta\right)\cos\frac{\theta}{2}+K^{II}\left(3\cos\theta-1\right)\sin\frac{\theta}{2}\right] \tag{1}$$

$$\sigma_{\theta\theta} = \frac{\cos\frac{\theta}{2}}{2\sqrt{2\pi r}}\left[K^{I}\left(1+\cos\theta\right)-3K^{II}\sin\theta\right] \tag{2}$$

$$\tau_{r\theta} = \frac{\cos\frac{\theta}{2}}{2\sqrt{2\pi r}}\left[K^{I}\sin\theta+K^{II}\left(3\cos\theta-1\right)\right] \tag{3}$$

where, K^{I} and K^{II} are mode I and II SIF in the direction of the crack/fault ($\theta = 0$), respectively. r is the distance from the crack tip and $\theta\left(-\pi \le \theta \le \pi\right)$ is the direction of an arbitrary plane at the crack tip with respect to x axis (Fig. 1). θ is positive counterclockwise and negative clockwise. The sign criterion of geomechanics is adopted, so compressive and tensile stresses are considered as positive and negative, respectively.

doi.org/10.1016/j.ijggc.2018.01.004

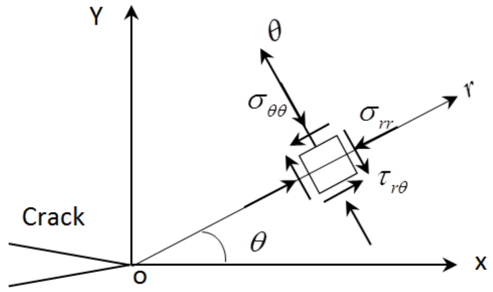

Fig. 1 Stress components at a point near a crack tip in the polar coordinate

The stresses are compressive in deep geological formations, so cracks/faults tend to be closed and the frictional resistance to be active. We assume a 2D plane-strain model in which the maximum and the minimum principal stress are contained in the in-plane direction and the intermediate stress is in the out-plane direction. Under compressive stresses, K^{I} and K^{II} for a crack with angle $0 \le \beta \le \pi/2$ (with respect to the horizontal line) can be obtained from (after Zhou et al., 2013)

$$K^{I} = \sigma_V \left(\cos^2\beta + \lambda \sin^2\beta\right)\sqrt{\pi a} \tag{4}$$

$$K^{II} = \left[\left(1-\lambda\right)\cos\beta\sin\beta - \left(-1\right)^{\delta}\mu\left(\cos^2\beta + \lambda\sin^2\beta\right)\right]\sigma_V\sqrt{\pi a} \tag{5}$$

$$\lambda = \frac{\sigma_h}{\sigma_V} \tag{6}$$

where σ_V and σ_h are the vertical and horizontal stresses, respectively, λ is stress anisotropy ratio, μ is the friction coefficient of the fault/crack plane and a is the half-length of the fault/crack. If $\sigma_V \ge \sigma_h$, $\delta = 0$, otherwise $\delta = 1$. This is done to ensure that the frictional force is in the opposite direction of the shearing force.

In fracture mechanics, the sign of K^{II} represents the direction of the mode II loading and it can be negative, positive or zero. $K^{II} = 0$ implies that no shearing is occurring on the crack. However, a different convention will be adopted in Section 2.2.

doi.org/10.1016/j.ijggc.2018.01.004

Positive values of K^{I} represent that the crack/fault surface closes and thus, a positive K^{I} is not physically meaningful. Positive values of K^{I} shown in the paper are only to compare its relative difference before and after injection.

Erdogan and Sih (1963) proposed the composite criterion of minimum circumferential tensile stress (minimum tensile–stress criterion). This criterion holds that a mixed mode I–II crack propagates along the corresponding direction of minimum tensile stress satisfying the following (modified after Wu et al., 2016)

$$\frac{\partial \sigma_{\theta\theta}}{\partial \theta} = 0, \quad \frac{\partial^2 \sigma_{\theta\theta}}{\partial \theta^2} > 0 \tag{7}$$

$$\theta^{IC} = 2\tan^{-1}\frac{1-\sqrt{1+8w^2}}{4w}, \quad w = \frac{K^{II}}{K^{I}} \tag{8}$$

where θ^{IC} is the corresponding direction of minimum tensile stress.

Mode I stress intensity factors in the direction of θ can be defined as (Rao et al., 2003)

$$K^{I}(\theta) = \lim_{r\to 0}\left(\sigma_{\theta\theta}\sqrt{2\pi r}\right). \tag{9}$$

The corresponding SIF of minimum tensile stress or equivalent mode I intensity factor is given by (modified after Wu et al. 2016)

$$K^{Ie} = \frac{1}{2}\cos\frac{\theta^{IC}}{2}\left[K^{I}\left(1+\cos\theta^{IC}\right) - 3K^{II}\sin\theta^{IC}\right]. \tag{10}$$

The fracture criterion for mode I crack grow/rupture is (Rao et al., 2003)

$$\left|K^{Ie}\right| \geq K^{IC}, \tag{11}$$

where K^{IC} is the fracture toughness in mode I.

Similarly, mode II stress intensity factor in the direction of θ can be defined as (Rao et al., 2003)

$$K^{II}(\theta) = \lim_{r\to 0}\left(\tau_{r\theta}\sqrt{2\pi r}\right). \tag{12}$$

To obtain the direction of maximum shear stress, the following condition should be satisfied

$$\frac{\partial \tau_{\theta r}}{\partial \theta} = 0,\ \left|\tau_{\theta r}\left(\theta = \theta_{\alpha}{}^{IIC}\right)\right|_{\max}. \tag{13}$$

This leads to a cubic equation with three roots. We derive the following solution as the corresponding direction of maximum (absolute value) shear stress

$$\theta_{\alpha}^{IIC} = 2\tan^{-1}\left(2\cos\left(\frac{g}{3}+(\alpha-2)\frac{\pi}{3}\right)\sqrt{-\left(\frac{p}{3}\right)}+\frac{w}{3}\right),\ \alpha = 1,2,3 \tag{14}$$

where, $p = -\frac{1}{3}(w)^2 - \frac{7}{2}$, $q = \frac{2}{27}(w)^3 - \frac{2}{3}w$, $g = \cos^{-1}\left(-\frac{1}{2}\frac{q}{\sqrt{-\left(\frac{p}{3}\right)^3}}\right)$ and α is the index of the three roots and only one of them maximizes the shear stress.

Therefore, the corresponding SIF of maximum shear stress or equivalent mode II intensity factor is given by (modified after Wu et al., 2016)

$$K^{IIe} = \frac{1}{2}\cos\frac{\theta^{IIC}}{2}\left[K^{I}\sin\theta^{IIC} + K^{II}\left(3\cos\theta^{IIC}-1\right)\right]. \tag{15}$$

The failure criterion for shear is given by (Rao et al., 2003)

$$\begin{cases}\left|K^{IIe}/K^{Ie}\right| \geq K^{IIC}/K^{IC} \\ K^{IIe} \geq K^{IIC}\end{cases}, \tag{16}$$

where K^{IIC} is the fracture toughness in mode II.

It must be noted that K^{I} in Eq. (10) and Eq. (15) is only meaningful if it is negative. Otherwise it should be set to zero.

2.2 Stress intensity factor path and critical overpressure

Similar to the stress path (Hettema et al., 2000), which is the change of total stress per change of unit pore pressure P inside the reservoir, it is possible to define the stress intensity path as

$$\kappa^{I} = \frac{\Delta K^{I}}{\Delta P}, \; \kappa^{II} = \frac{\Delta K^{II}}{\Delta P} \tag{17}$$

for mode I and mode II, respectively. In contrast to stress path, stress intensity path is not independent of the stress regime (Gheibi et al., 2016, 2017). However, κ is constant for a given fault placed at a particular location in a given stress regime even for different stress anisotropy ratios λ (as will be discussed in section 3.1). Therefore, if κ is known for a fault, it is possible to find the minimum and the maximum K for mode I and II, respectively, corresponding to the direction of minimum tensile and maximum shear stress. This can be used to find the critical pressure change above which mode I or mode II rupture of the fault could be initiated. Actually, there are no explicit solutions to relate the critical pressure to the critical toughness values. However, we propose some relations by which variations of SIF as a function of pressure change can be plotted to find the critical pressure.

The application of the relationships developed in Section 2.1 becomes slightly different when using the κ defined in Eq. (17). Here, it is assumed $K^{II} < 0$ for a stable and $K^{II} > 0$ for an unstable fault. This assumption is made to provide a ground for general definition of the stress intensity path in Eq. (17) independent of the overpressure magnitude. For example, consider a given fault that is initially stable. Based on the convention in fracture mechanics, the K^{II} should be set to zero. Assuming that the fault is still stable after an overpressure of some MPa, so we should set the K^{II} to be zero again. In such condition, if we define the stress intensity path for the fault, it is equal to zero. However, if the pressure is increased to a certain value that the fault becomes unstable, K^{II} turns non-zero and the stress intensity path will become a finite positive value if $\sigma_V > \sigma_h$ and negative if $\sigma_V < \sigma_h$. Therefore, it is not possible to define a general stress intensity path and it is changed for different overpressure level. However, if we impose that for a stable and unstable fault the $K^{II} < 0$ and $K^{II} > 0$,

doi.org/10.1016/j.ijggc.2018.01.004

respectively, we can ensure that the $\Delta K^{II}/\Delta P$ is independent of the overpressure magnitude for a given fault.

δ is used to ensure that K^{II} is positive for unstable faults independently of the shearing direction. Thus, in this paper, a negative value of K^{II} implies that the fault/crack is stable and cannot propagate. Nevertheless, the negative K^{II} shown in the Results (Tables 2 and 3) are only to compare the relative difference of K^{II} before and after injection to calculate the SIF changes. In the rest of this section, the procedure to analyze the rupture propagation of a fault will be given using k.

The direction of the minimum tensile stress after a pressure change can be obtained using Eq. (8) as follows

$$\theta_f{}^{IC} = \theta^{IC}\Big|_{w=\overset{*}{w}}, \ \overset{*}{w} = \left(\frac{K_i^{II} + \kappa^{II}\Delta P}{K_i^{I} + \kappa^{I}\Delta P}\right) \tag{18}$$

where subscripts *f* and *i* represent the final and initial state, respectively. The initial K values can be calculated either numerically (as discussed in Section 2.4) or using Eqs. (4) and (5). $K_i^I + \kappa^I \Delta P$ should be negative, otherwise it should be set to zero. Also, if $K_i^{II} + \kappa^{II}\Delta P$ is negative, it means that the fault is stable and the analyses are no longer meaningful.

The final $K_f{}^{Ie}$ is calculated by combining Eq. (10), Eq. (17) and Eq. (18) as

$$K_f{}^{Ie} = K_i{}^{Ie} + \frac{1}{2}\cos\frac{\theta_f{}^{IC}}{2}\left[\kappa^I\left(1+\cos\theta_f{}^{IC}\right) + 3(-1)^{\delta}\left(\kappa^{II}\right)\sin\theta_f{}^{IC}\right]\Delta P \tag{19}$$

Note that Eq. (19) is a nonlinear relationship, because $\theta_f{}^{IC}$ is also dependent on ΔP. Since, an analytical solution was not found for ΔP, the $\Delta P^I_{crit.}$ should be obtained by plotting $K_f{}^{Ie}$ vs ΔP combined with $K_f{}^{Ie} = K^{IC}$.

Likewise, the relationship between the pressure change and the direction and magnitude of the maximum Mode II SIF after injection is given by combining Eq. (14), Eq. (15) and Eq. (17) as

doi.org/10.1016/j.ijggc.2018.01.004

$$\theta_f^{IIC} = \theta^{IIC}\Big|_{w=\overset{*}{w}} \qquad \overset{*}{w} = \left(\frac{K_i^{II} + \kappa^{II}\Delta P}{K_i^{I} + \kappa^{I}\Delta P}\right) \tag{20}$$

$K_i^I + \kappa^I \Delta P$ should be negative, otherwise it should be set to zero. Also, if $K_i^{II} + \kappa^{II}\Delta P$ is negative, it means that the fault is stable and the analyses are no longer meaningful. The final K_f^{IIe} is calculated by combining Eq. (15), Eq. (17) and Eq. (20) as

$$K_f^{IIe} = K_i^{IIe} + \frac{1}{2}\cos\frac{\theta_f^{IIC}}{2}\left[\kappa^I \sin\theta_f^{IIC} - (-1)^{\delta}\left(\kappa^{II}\right)\left(3\cos\theta_f^{IIC} - 1\right)\right]\Delta P\ . \tag{21}$$

Similarly, K_f^{IIe} and ΔP are non-linearly related. The critical overpressure $\Delta P_{crit.}^{II}$ can be obtained by plotting K_f^{IIe} vs ΔP combined with $K_f^{IIe} = K^{IIC}$ for mode II rupture if Eq. (16) is satisfied. The final critical overpressure for injection is $\Delta P_{crit.} = \min\left(\Delta P_{crit.}^{I}, \Delta P_{crit.}^{II}\right)$.

It must be noted that if $\left[K_i^{Ie} + \frac{1}{2}\cos\frac{\theta_f^{IC}}{2}\left[\kappa^I\left(1+\cos\theta_f^{IC}\right)\right]\Delta P\right] > 0$, only the κ^{II} part must be considered in the calculations in Eq. (19) and Eq. (21).

2.3. Modified Discrete Element Method

The Modified Discrete Element Method (MDEM) was proposed by Alassi (2008) to model fracture developments and fault reactivation during fluid withdrawal and injection at reservoir scale. MDEM behaves like a continuum model (e.g., finite element method) before failure and like a discontinuum model (e.g., discrete element method) after failure.

The mesh of MDEM considers the continuum to be formed by discrete particles, which are usually assumed to be circular (Itasca 2012). However, they can follow Voronoi's shape, which makes it easier to build more complicated models with the help of automatic mesh generation codes (Fig. 2b). Fig. 2a shows a triangular element formed by connecting the centers of three discs which are in contact two by two. The triangle element is also called a cluster. The discrete element method uses a

doi.org/10.1016/j.ijggc.2018.01.004

simple constitutive relationship that relates the internal forces to the relative displacements at the contact as

$$\mathbf{f_n} = \mathbf{D_n u_n} \tag{22}$$

$$\mathbf{f_s} = \mathbf{D_s u_s} \tag{23}$$

where $\mathbf{f}$, $\mathbf{D}$ and $\mathbf{u}$ are internal force, stiffness and relative displacement of contact, respectively. The subscripts n and s represent normal and shear components.

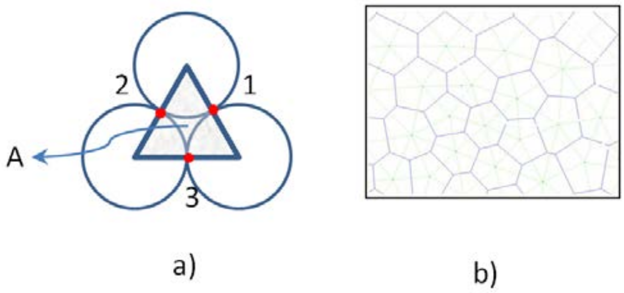

Fig. 2 Representation of MDEM using a) circular and b) Voronoi's element (Alassi, 2008)

Eq. (24) shows the constitutive relationship of the normal forces and the normal relative displacements of the three contacts of a cluster (Fig. 2b). The shear contact force is neglected by setting the contact shear stiffness to zero, i.e., $D_s = 0$. Then, the modification of the original discrete element method is done by adding new stiffness coefficients a_{ij}.

$$\begin{Bmatrix} f_{n1} \\ f_{n2} \\ f_{n3} \end{Bmatrix} = \begin{pmatrix} D_{n1} & a_{12} & a_{13} \\ a_{21} & D_{n2} & a_{23} \\ a_{31} & a_{32} & D_{n3} \end{pmatrix} \begin{Bmatrix} u_{n1} \\ u_{n2} \\ u_{n3} \end{Bmatrix}. \tag{24}$$

a_{ij} represents the contribution of the deformation of j^{th} contact on the force of i^{th} contact.

The relationship between the stress $\boldsymbol{\sigma} = \{\sigma_{xx} \quad \sigma_{yy} \quad \sigma_{xy}\}^T$ and the internal forces $\mathbf{f_n}$ and the relation between the strain $\boldsymbol{\varepsilon} = \{\varepsilon_{xx} \quad \varepsilon_{yy} \quad \varepsilon_{xy}\}^T$ and the relative displacements $\mathbf{u_n}$ are given by

$$\boldsymbol{\sigma} = \frac{1}{A}\mathbf{M}^{\mathrm{T}}\mathbf{f}_{\mathbf{n}} \quad (25)$$

$$\mathbf{u}_{\mathbf{n}} = \mathbf{M}\boldsymbol{\varepsilon} \quad (26)$$

where A is the area of the cluster (triangle) and $\mathbf{M}$ is the unit normal vector matrix defined as

$$\mathbf{M} = \begin{pmatrix} e^2{}_{11}l_1 & e^2{}_{12}l_1 & e_{11}e_{12}l_1 \\ e^2{}_{21}l_2 & e^2{}_{22}l_2 & e_{21}e_{22}l_2 \\ e^2{}_{31}l_3 & e^2{}_{32}l_3 & e_{31}e_{32}l_3 \end{pmatrix}, \quad (27)$$

where $e_{h1} = \cos(\theta_h)$, $I_{h2} = \sin(\theta_h)$ and the angle θ_h represents the normal vector orientation of the contact h inside the cluster, l_h is the contact length (the distance between the centers of the two particles or centers of Voronoi elements that are in contact), and h is the number of contacts. The stress can be related to the strain by using the material conventional constitutive elastic matrix $\mathbf{C}$ as

$$\boldsymbol{\sigma} = \mathbf{C}\boldsymbol{\varepsilon}\,. \quad (28)$$

Combining Eqs. (24)– (28), a relation can be derived between the internal constitutive matrix $\bar{\mathbf{D}}$ and the material constitutive matrix $\mathbf{C}$ as

$$\mathbf{C} = \frac{1}{A}\mathbf{M}^{\mathrm{T}}\bar{\mathbf{D}}\mathbf{M}\,. \quad (29)$$

Once $\bar{\mathbf{D}}$ has been retrieved from Eq. (29), the solution scheme is similar to the regular discrete element method. In this method, the contact forces are updated incrementally, $d\mathbf{f}_{\mathbf{n}} = \bar{\mathbf{D}}\,d\mathbf{u}_{\mathbf{n}}$ and $\mathbf{f}_{\mathbf{n}}{}^{new} = \mathbf{f}_{\mathbf{n}} + d\mathbf{f}_{\mathbf{n}}$, where $d\mathbf{u}_{\mathbf{n}}$ at each contact is calculated by using the Voronoi element's velocities $\mathbf{v}_i$ and the time step dt as

$$d\mathbf{u}_{\mathbf{n}} = \left(v^1{}_i - v^2{}_i\right)e_i dt\,, \quad (30)$$

where the superscripts 1 and 2 represent the centers of the two disks forming a contact and the subscript i is the i[th] component of the velocity vector. Then, the forces are applied to each particle and Newton's second law is used to update the particle's motion (see Cundall and Strack (1979) for more details).

For a failing cluster, both $\mathbf{D_n}$ and $\mathbf{D_s}$ are used to update the normal and the shear forces at each contact and thus a shear contact force $\mathbf{f_s}$ starts to build up in the failing cluster and at each contact according to $d\mathbf{f_s} = \mathbf{D_s} d\mathbf{u_s}$, where $d\mathbf{u_s}$ is calculated as

$$d\mathbf{u_s} = \left|\Delta\mathbf{v}_i - \Delta\mathbf{v}_j\mathbf{I}_j\mathbf{I}_i\right| dt, \tag{31}$$

where $\Delta\mathbf{v}_i = \left(v_i^1 - v_i^2\right)$ is the relative velocity and I_i is the normal unit vector. Notice that Einstein summation convention with dummy subscript i, j is used in Eq. (31).

This means that $\mathbf{D_s}$ will be zero before failure occurs but will have a finite value after failure to model the shear stress that is developed at the cracks' interfaces. The new stiffness coefficient a_{ij} introduced in Eq. (24) is deleted at this stage and contact separation is allowed, which will weaken the failing cluster and cause the stress to redistribute. A fault is a collection of failed clusters which has two contacts failed ($\mathbf{D}_s$ and $\mathbf{D}_n$ are thus updated). The direction of the failed contact is updated to the direction of the fault. This is equivalent to the smooth-joint model in DEM introduced by Mas Ivars et al. (2008).

The main difference between this approach and the regular discrete element method is that while the material can behave according to a continuum model before failure, where conventional elastic properties can be given to the material based on Eq. (29), the material behaves according to a regular discrete element method after failure.

2.4. Calculation of K^I and K^{II} in MDEM

Consider a cracked isotropic body subjected to mixed-mode I - II loadings under plane stress or plane strain conditions. The crack is assumed to be oriented along an arbitrary direction. Therefore, stresses along the x-axis and in the vicinity of the crack tip are

$$\sigma_{yy} = \frac{K^I}{\sqrt{2\pi x}} , \tag{32}$$

$$\tau_{xy} = \frac{K^{II}}{\sqrt{2\pi x}}, \tag{33}$$

The total forces over the x^c-sized ligament (Fig. 3) can be expressed as (de Morais 2007)

$$F_y = \int_0^{x_c} \sigma_{yy} dx = K^I \sqrt{\frac{2x^c}{\pi}} , \tag{34}$$

$$F_x = \int_0^{x_c} \tau_{xy} dx = K^{II} \sqrt{\frac{2x^c}{\pi}} , \tag{35}$$

and their values can be evaluated from the internal forces of the contacts for a cluster at its center of gravity as shown in Fig. 3. x_i^c is the distance between the crack tip and the center of mass of each of the triangle elements in front of the crack tip in the *x*-direction.

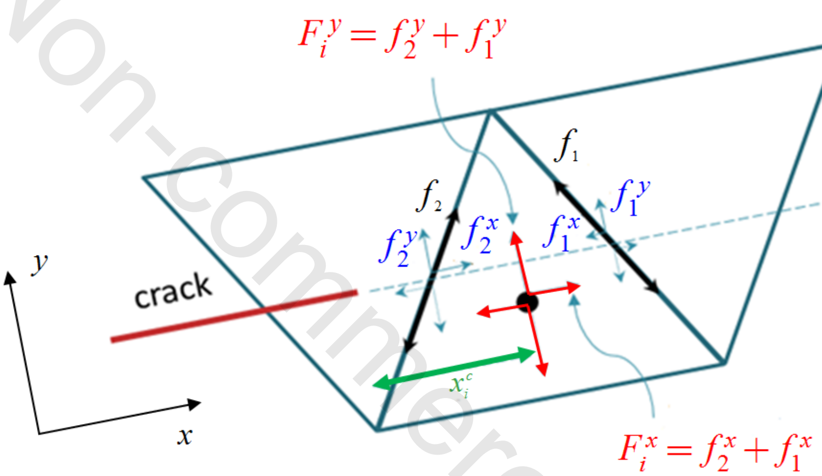

Fig. 3 A pre-existing crack and clusters in front of the crack tip and calculation of forces required to determine K^I and K^{II}

SIF estimation formulae are

$$K^{*I} = \sqrt{\frac{\pi}{2x_i^c}} \sum_{i=1}^{l} F_i^y , \tag{36}$$

$$K^{*II} = \sqrt{\frac{\pi}{2x_i^c}} \sum_{i=1}^{l} F_i^x , \tag{37}$$

K^I and K^{II} are calculated by extrapolating to $x^c = 0$ of the linear approximations to K^{*I} and K^{*II} as a function of x^c plots, respectively. Fig. 4 shows an example of approximating K^I and K^{II} of a simple horizontal crack. The deviation from the analytical K^I and K^{II} values is about 1%.

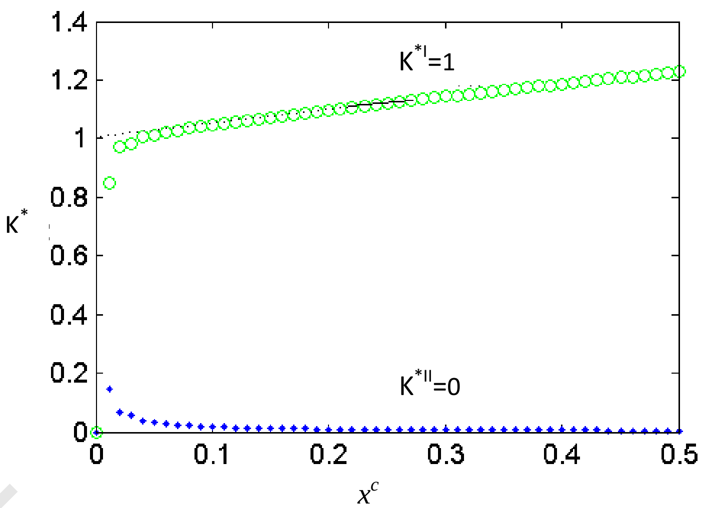

Fig. 4 Linear approximations to K^{*I} and K^{*II} as a function of x^c and extrapolating to $x^c = 0$ for a central horizontal crack

2.5. Numerical model

Fig. 5 shows a schematic description of the general 2D plane-strain model used in this study. The smallest elements are equilateral triangles with sides equal to 1.1 m. Actually, coarser elements could be used obtaining similar results. The aim of the analyses is not to perfectly model CO_2 injection, but rather to understand how faults rupture is affected by reservoir pressurization. Therefore, no fluid flow modeling is carried out. Instead, the reservoir is assumed to be a closed box surrounded by impermeable rock and pore pressure is increased uniformly inside the reservoir by ΔP. Such assumption may be acceptable for small and closed reservoirs, which may be common in CO_2-EOR or in certain saline formations that are bounded by low-permeable faults, like Snohvit, in which pressure buildup increased rapidly as a result of the small size of the reservoir and led to the stop of injection a few months after the beginning of CO_2 injection to avoid fault reactivation (Hansen et al., 2013).It is also assumed that the pore pressure remains constant and equal to the initial value in the surrounding rock, including the caprock. The reservoir lateral edges are assumed to be half-circles (semicircles) to avoid a high stress concentrations due to sharp boundary effects and thus, to have a simple stress distribution in the models. This helps to understand the results more clearly. Two faults are represented in Figure 5, one in the center of the reservoir, placed at (0, 0), and the other one in the caprock above the right-hand side flank, at (400,250). The points correspond to the coordinates of the faults center (shown by dots in Fig. 5). The locations of the faults analyzed in the scenarios considered in the paper are not necessarily identical to the ones in Fig. 5 (see Table 1). The reservoir thickness is 200 m and the aspect ratio of most of the models is 0.25. Fault length is 100 m, unless otherwise stated. The mechanical boundary conditions are a constant stress equal to the far-field stresses in most of the models. The maximum principal stress is considered to be in the vertical and the horizontal directions in an extensional (normal faulting) and a compressional (reverse faulting) stress regime, respectively. Stress anisotropy ratio λ, is varied to be 0, 0.2, 0.33, 0.5 and 1. $\lambda = 0$ is representative of uniaxial tests without lateral confinement. The stress intensity factor values are given in K' normalized to $\sigma_1\sqrt{50\pi}\left(MPa.m^{-0.5}\right)$ in the results. Therefore, the results can be used for any initial *in situ* stress value. Additionally, a model is run in which the vertical stress is the weight of the layers above the reservoir (gravity effect), assuming that the lateral boundaries are fixed (displacement is not allowed). In this gravity model, the center of the reservoir is placed at 1.5 km depth. In the gravity case, λ depends on Poisson's ratio. The initial and post-injection horizontal stresses evolve due to the Poisson's ratio effect in a fixed lateral displacement. This leads to a horizontal stress that is lower than the weight of the layers on top. Therefore, the stress regime in this situation is extensional.

Table 1 summarizes the model parameters for the several scenarios investigated in the paper indicating the subsections in the Results in which they are used. In the base case model, the elastic constants are

doi.org/10.1016/j.ijggc.2018.01.004

the same for the reservoir and the surrounding rock with $E_r = E_s = 15GPa$ and $\nu_r = \nu_s = 0.2$, where E is the Young's modulus and ν is the Poisson's ratio. The subscripts r and s refers to reservoir and surrounding, respectively. Other Poisson's ratio values are also used in Section 3.5 (see Table 1). The pore pressure increase is assumed to be 10 MPa inside the reservoir, unless otherwise stated. Since stress intensity path is given for unit pore pressure change, the results can be applied for other pore pressure values as well. The faults in all the scenarios are investigated in separate models, thus, there is no interaction between them, except in Section 3.6 where the effect of one fault on the other is investigated.

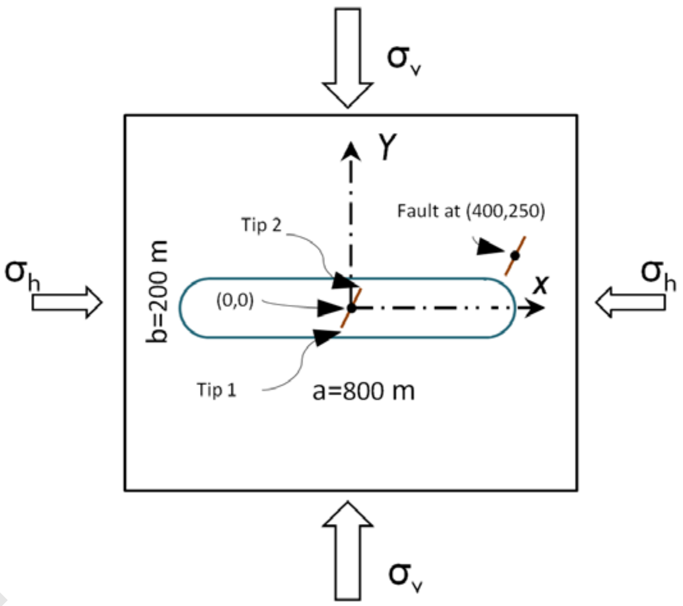

Fig. 5 Schematic representation of the general model, which includes two faults

Table 1. Parameters used to model the investigated scenarios. E, C, G and (x, y) represent Extensional, Compressional, Gravity and coordinates of the faults center, respectively.

Section no.	Fault dip (°)	Stress regime	ν_r	ν_s	Fault length (m)	Fault center		Aspect ratio	Fault interaction
3.1	60	E-C-G	0.2	0.2	100	X	0	0.25	No
						Y	0, 250		
3.2	60	E-C	0.2	0.2	100	X	0, 200, 400, 600	0.25	No
						Y	0, 175, 250		
3.3	60	E	0.2	0.2	300, 400, 500	X	0, 200, 400, 600	0.25	No
						Y	0		
3.4	20, 30, 60, 70	E-C	0.2	0.2	100	X	0, 200, 400, 600	0.25	No
						Y	0, 250		

3.5	1st set	70	E-C	0.1, 0.2,0.3	0.2	100	X	0, 200, 400, 600	0.25	No
							Y	0		
	2nd set			0.2	0.1, 0.2,0.3	100	X	0, 200, 400, 600		
	3rd set			0.1, 0.2,0.3	0.2		Y	250		
3.6		70	E-C	0.2	0.2	50, 100, 200, 300	X	0, 200	0.25	Yes
							Y	250		
3.7		30, 70	E-C	0.2	0.2	100	X	0, 200, 400, 600	0.125, 0.167, 0.25	No
							Y	0, 250		

3. Results

3.1. Injection induced stress intensity path

Stress intensity factor for a given fault/crack is determined based on the stresses applied on it. Changes in pore pressure inside the reservoir will induce new stresses and therefore, the stress intensity path is directly related to the poroelastic stress changes. As an illustrative example of how a uniform 10 MPa pressure increase in a closed reservoir causes stress changes, Fig. 6 shows the distribution of the change in total stresses in the *x*- and *y*- direction for the base case model without any fault. Details about the stress changes caused by reservoir pressurization can be found in Gheibi et al. (2017). If faults are present, the stress distribution is affected by their presence, which influences the results. The proposed methodology automatically takes these stress changes into account.

Table 2 summarizes the SIF calculated for different stress scenarios in the initial and post-injection conditions as well as the SIF path for a fault with dip of 60° and a length of 100 m crossing the reservoir center. The whole length of the fault is inside the reservoir, because the thickness of the reservoir is 200 m (Fig. 5). κ^{I} is negative and equal in all the λ scenarios for the fault, except in the gravity-uniaxial strain case, in which the κ^{I} is slightly greater, i.e., closer to zero. This means that the κ^{I} will decrease (to a more tensile mode) inside the reservoir due to the overpressure, increasing the chance of mode I fault propagation. However, κ^{II} is positive, presenting a lower value in an extensional stress regime than in a compressional stress regime. This implies that the fault inside the reservoir is less likely to propagate in mode II in an extensional regime compared to a compressional stress regime after injection. While κ^{II} in the isotropic stress condition is almost equal to its value in a

doi.org/10.1016/j.ijggc.2018.01.004

compressional stress regime, κ^{II} in an extensional stress regime is similar to the κ^{II} in the gravity case, which is also an extensional stress regime.

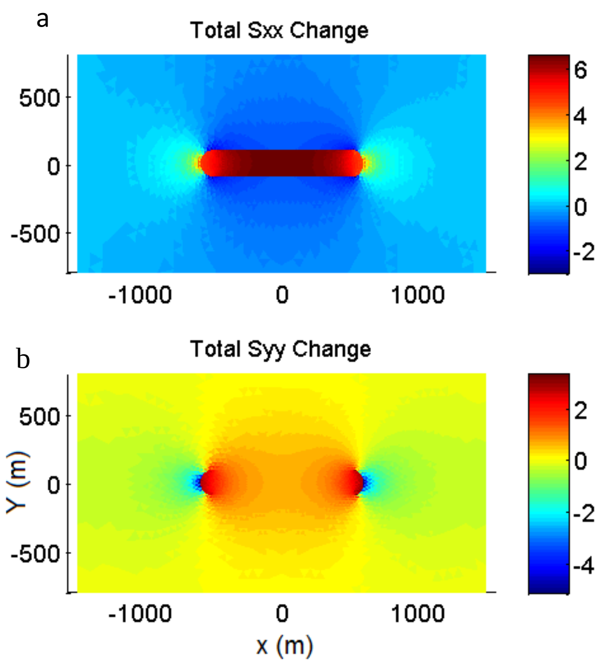

Fig. 6 Distribution of the total stress change (MPa) in a) *x*- b) *y*- directions induced by a 10 MPa increase in the reservoir pore pressure

Table 3 represents $K^{'}$ and κ values for the same scenarios as in Table 2, but with a fault placed in the caprock, at (0, 250). Similar to the fault in the reservoir, κ^{I} decreases in the caprock, but, the magnitude is almost 1/10th of that in the reservoir. κ^{II} increases in extensional and isotropic stress regimes, but it decreases in a compressional stress regime. Therefore, a steep fault in the caprock is less likely to propagate in mode II due to reservoir pressurization in a compressional stress regime.

Table 2- Calculation of the initial and post-injection SIF ($K^{'}$) and change in SIF (κ) for a fault with dip angle of 60° crossing the reservoir for several stress anisotropy ratios (λ) after a pore pressure increase of 10 MPa in the reservoir. The $K^{'}$ values are normalized with respect to $\sigma_1\sqrt{50\pi}\left(MPa.m^{-0.5}\right)$. For the gravity case, σ_1 is assumed to be 30 MPa. The subscripts *i* and *f* represent initial and final, respectively.

Stress Regime	λ	$K^{'\,I}_{i}$	$K^{'\,II}_{i}$	$K^{'\,I}_{f}$	$K^{'\,II}_{f}$	κ^{I}	κ^{II}
Isotropic stress	1	1.01	-0.59	0.86	-0.43	-6.43	6.60
Extensional	0.5	0.63	-0.16	0.46	-0.14	-6.43	1.12
	0.3	0.51	-0.01	0.34	0.01	-6.43	1.12
	0.2	0.41	0.105	0.23	0.13	-6.43	1.12
	0	0.25	0.28	0.08	0.31	-6.43	1.12

Compressional	0	0.76	-0.02	0.59	0.15	-6.43	6.59
	0.2	0.81	-0.13	0.64	0.04	-6.43	6.60
	0.3	0.85	-0.21	0.68	-0.04	-6.43	6.59
	0.5	0.89	-0.31	0.72	-0.14	-6.43	6.59
Gravity U. Strain	0.33	0.54	0.06	0.37	0.09	-6.18	1.00

Table 3- Calculation of initial and post-injection SIF (K') and change in SIF (κ) for a fault with dip angle of 60° in the caprock for several stress anisotropy ratios (λ) after a pore pressure increase of 10 MPa in the reservoir. The K' values are normalized with respect to $\sigma_1\sqrt{50\pi}\left(MPa.m^{-0.5}\right)$. For the gravity case, σ_1 assumed to be 30 MPa.

Stress Regime	λ	K'^{I}_{i}	K'^{II}_{i}	K'^{I}_{f}	K'^{II}_{f}	κ^{I}	κ^{II}
Isotropic stress	1	0.99	-0.59	0.97	-0.56	-0.61	1.34
Extensional	0.5	0.62	-0.15	0.60	-0.12	-0.62	1.34
	0.3	0.49	-0.01	0.48	0.02	-0.61	1.34
	0.2	0.40	0.10	0.38	0.14	-0.61	1.34
	0	0.25	0.28	0.23	0.31	-0.61	1.34
Compressional	0	0.74	-0.02	0.72	-0.03	-0.61	-0.60
	0.2	0.79	-0.13	0.77	-0.15	-0.61	-0.61
	0.3	0.82	-0.21	0.80	-0.23	-0.61	-0.61
	0.5	0.86	-0.31	0.84	-0.32	-0.61	-0.61
Gravity U. Strain	—	0.46	0.08	0.45	0.11	-0.53	1.26

3.2. Effect of fault location

The effect of the location of a fault with dip angle of 60° placed inside the reservoir on κ is investigated by placing the center of the fault, at locations (0, 0), (200, 0), (400, 0). Additionally, a fault is placed at (600, 0) at the right-hand side flank, outside of the reservoir. Fig. 7 represents the variation of κ at the two fault tips as a function of the location of the fault in an extensional and a compressional stress regime. κ^{II} increases considerably inside the reservoir, but only slightly in the flank. The maximum value is recorded for the fault at the reservoir center in a compressional regime. κ^{II} gradually approaches to zero as the fault moves away from the reservoir center. However, in an extensional regime, it increases in the central parts of the reservoir and decreases in the rest, reaching negative values in the flank outside of the reservoir. For both fault tips (Fig. 5), κ^{II} almost coincides everywhere, except for the case in which the fault center is located at the reservoir boundary, i.e., (400, 0). For this case, tip 1 lies inside the reservoir but tip 2 is placed outside of it. The tip 2 experiences a

doi.org/10.1016/j.ijggc.2018.01.004

greater change in κ^{II} presenting a greater decrease (more stable) and increase (less stable) in an extensional and a compressional regime, respectively (Fig. 7b). On the other hand, κ^{I} decreases inside the reservoir and increases outside the reservoir in the flank, so tensile failure is can only occur inside the reservoir.

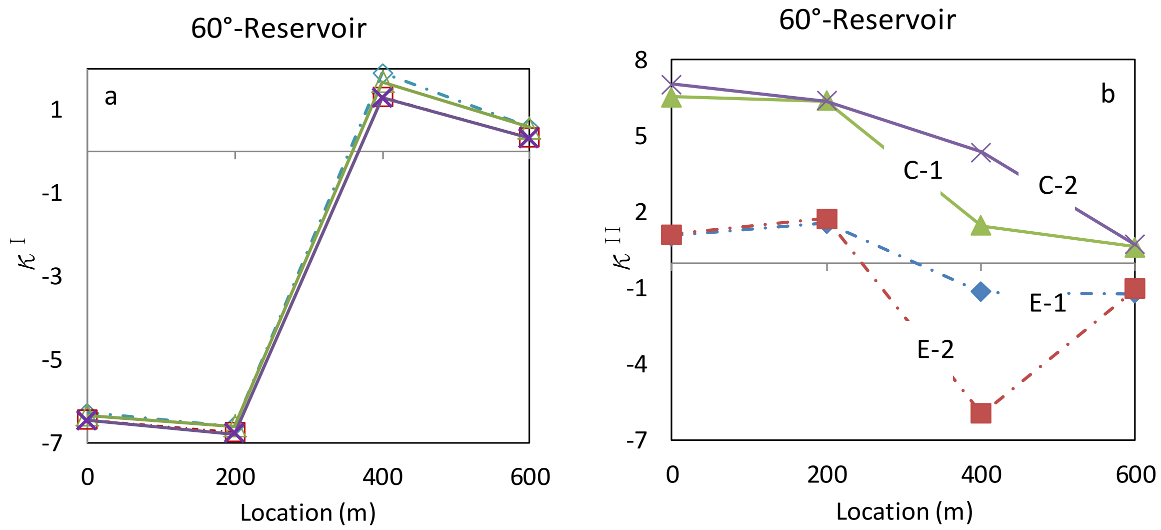

Fig.7 Variation of a) κ^{I} b) κ^{II} as a function of the location of the center for the two tips of a fault with a dip angle of 60° inside the reservoir and its flank in a compressional (C) and an extensional (E) stress regime. 1 and 2 refer to the tip number, as indicated in Fig. 5

The effect of fault location is also analyzed in the caprock at two horizontal sections placed at a vertical distance from the reservoir center of 175 m and 250 m. Fig. 8 shows κ^{I} and κ^{II} as a function of the locations of the faults centers. κ^{I} decreases (negative) in all of the investigated locations and the greatest decrease in mode I stability occurs for the fault located at (400, 175), i.e., the fault placed above the reservoir flank in the caprock and that is closer to the reservoir-caprock interface. κ^{I} in the caprock is almost identical in the two stress regimes. κ^{II} increases above the reservoir and decreases above the flanks in an extensional regime, but the opposite occurs in a compressional stress regime. The greatest shear rupture risk occurs in the caprock above the reservoir and in the caprock above the flanks in an extensional and a compressional regime, respectively.

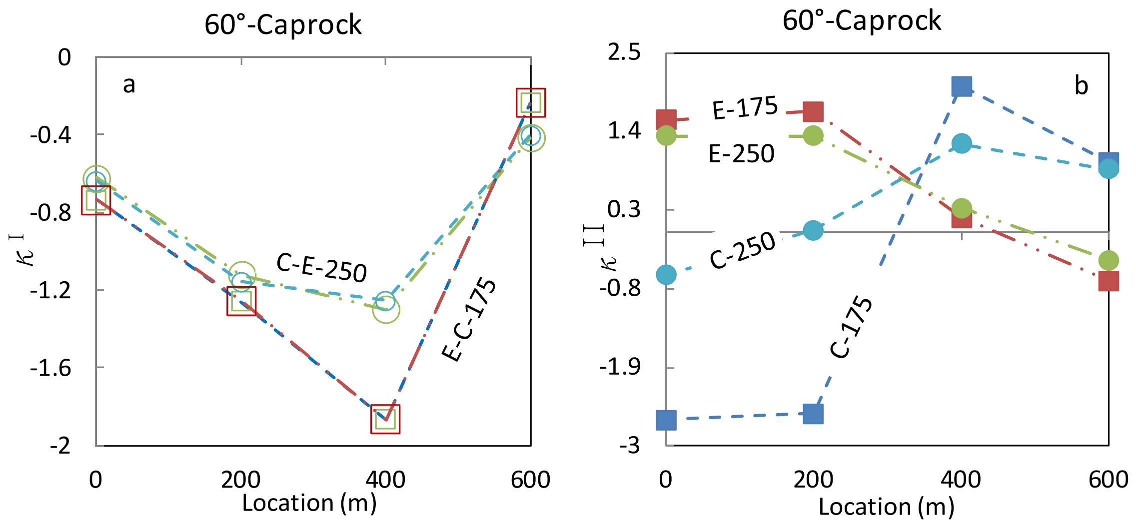

Fig. 8 Variation of a) κ^I b) κ^{II} as a function of the location of the center of a fault with dip angle of 60° in the caprock (fault centers placed at y=175 and 250 m) in a compressional (C) and an extensional (E) stress regime

3.3. Effect of fault length

Fig. 9 shows κ^I and κ^{II} as a function of the location in the *x*-axis of three faults with a dip angle of 60° with their centers placed in the reservoir horizontal axis with length equal to 300, 400 and 500 m in an extensional stress regime. While the central portion of the faults stays inside the reservoir, the two tips are in the over- and under-burden. The shorter the fault, the greater the decrease in κ^I in the central part of the reservoir. The reason for this is that the reduction of the horizontal total stress in the caprock is greater as it gets closer to the reservoir. However, the longer faults present a greater in κ^{II} in the reservoir.

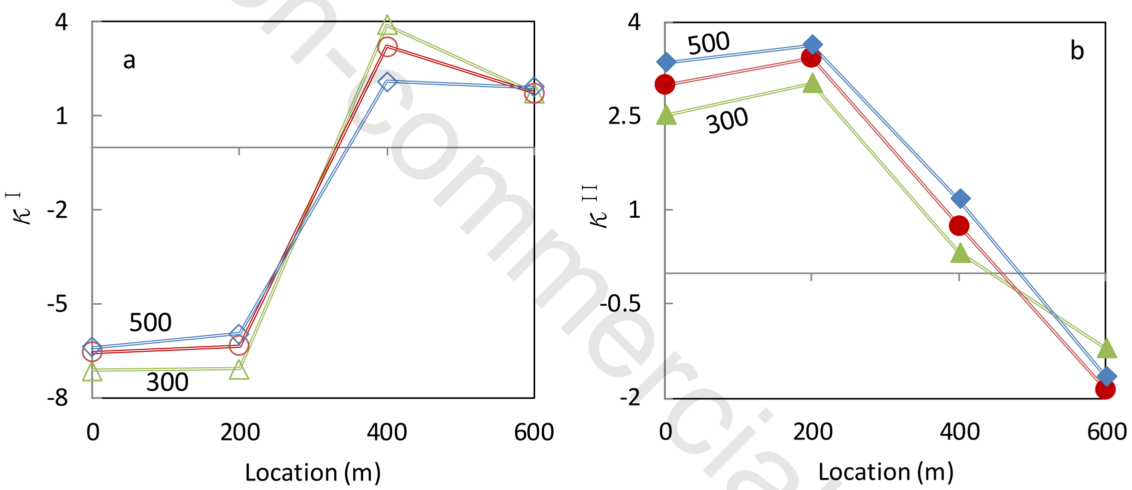

doi.org/10.1016/j.ijggc.2018.01.004

Fig. 9 Variation of a) κ^{I} b) κ^{II} as a function of the location of the center of a fault with a dip angle of 60° and with three lengths of 300, 400 and 500 m in an extensional stress regime

3.4. Effect of fault dip angle

A fault with length of 100 m and dip angles of 20°, 30°, 60° and 70° is modeled placed at points (0,0), (200,0), (400,0) and (600,0) in the reservoir and the flanks and (0,250), (200,250), (400,250) and (600,250) in the caprock. Fig. 10 represents the variation of κ^{I} and κ^{II} as a function of the location of the faults with different dip angles in both a compressional and an extensional stress regime. The κ^{I} is almost identical in all cases regardless of the stress regime and becomes lower (higher propensity for tensile failure) for the less steep faults. Also, κ^{II} has a greater value as the fault dip angle decreases in the two stress regimes except for the 30° fault in a compressional stress regime, which has slightly higher κ^{II} than the 20° fault.

Fig. 10 indicates that the faults with lower dip angle are more prone to propagate than the faults with higher dipping angle both in mode I and mode II in the central parts of the reservoir. This is due to the fact that the change in the horizontal stress, which tends to close the steeper fault plane, is greater than that in the vertical stress.

Fig. 11 shows κ^{I} and κ^{II} variation of the same faults as a function of the location of the fault center for the faults placed in the caprock, 250 m above the reservoir center, in a compressional and an extensional stress regime. Contrary to the faults inside the reservoir, the obtained κ^{I} is lower for high dip angle faults than for low dip angle faults (Fig. 11a). This implies that steeper faults in the caprock are under a higher risk of mode I propagation due to reservoir pressurization. In contrast to κ^{II} variation of the faults in the reservoir and the flank, in the caprock the higher the dip angle, the greater κ^{II} in a compressional regime (Fig. 11b). In an extensional regime, κ^{II} is greater for high dip angle faults in the central parts, but lower above the flank in the caprock (Fig. 11c).

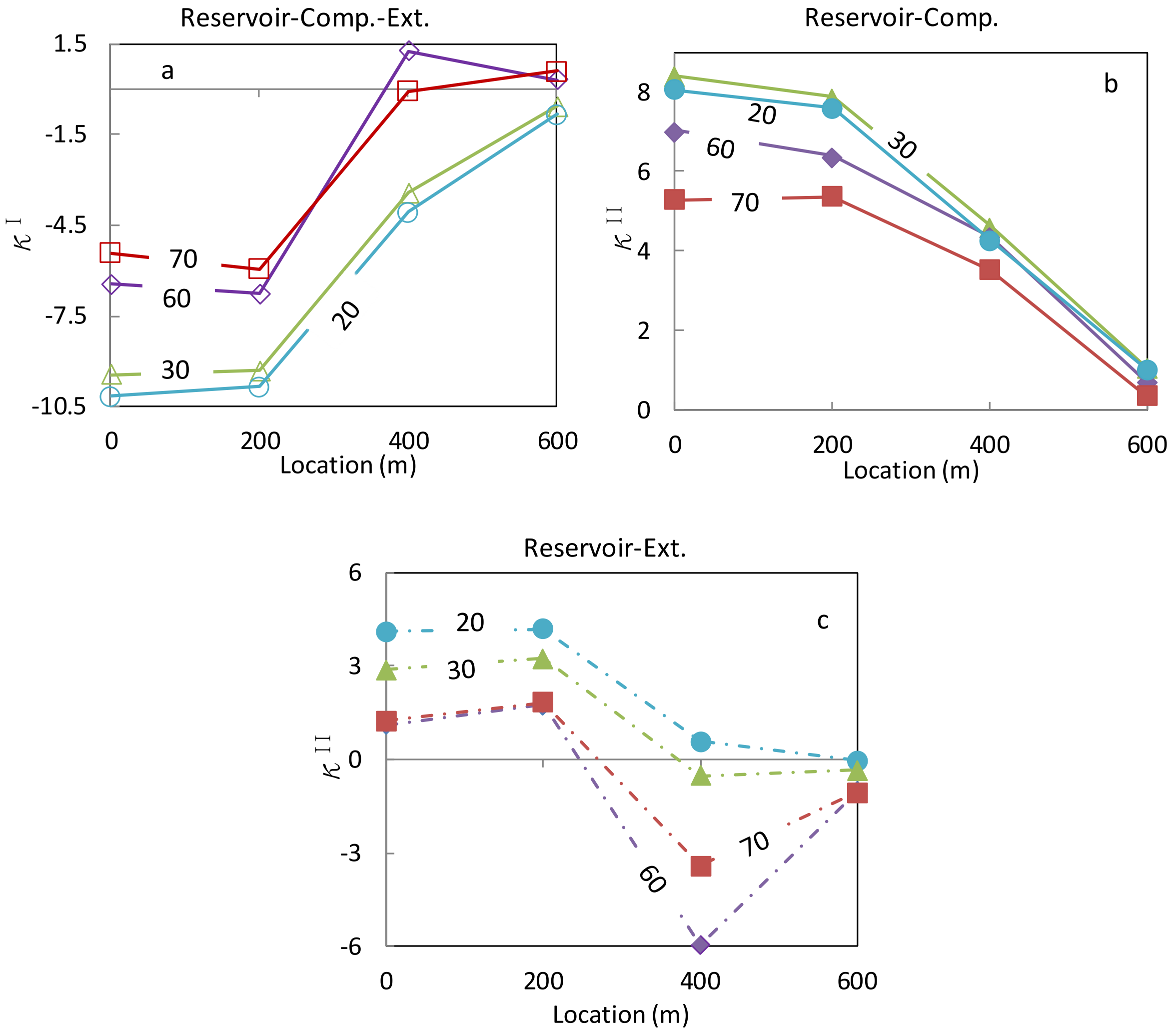

Fig. 10 Variation of a) κ^{I}, b) κ^{II} and c) κ^{II} as a function of the location of the center of faults with different dip angles in the reservoir and flanks in a compressional and an extensional stress regime

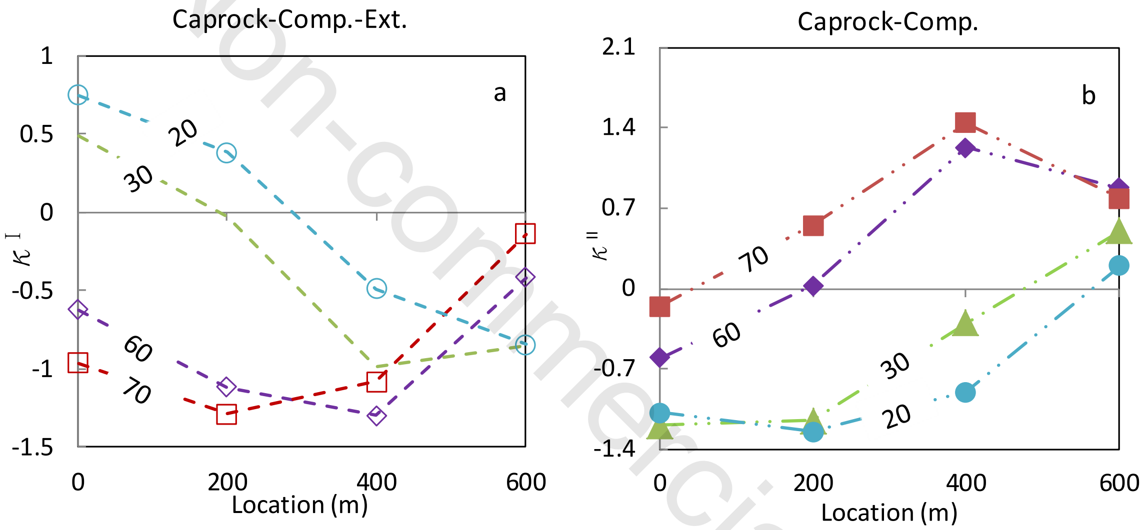

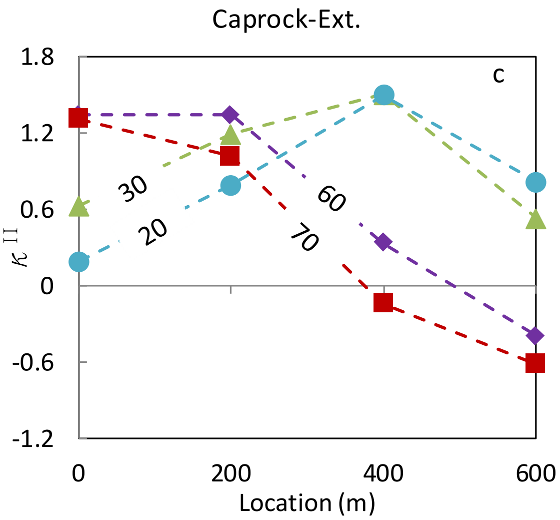

Fig.11 Variation of a) κ^{I} , b) κ^{II} and c) κ^{II} as a function of the location of the center of faults with different dip angles in the caprock (y=250m) in a compressional and an extensional stress regime

3.5. Effect of Poisson's ratio

Fig. 12 shows κ variation as a function of the location of the center of a fault with dip angle of 70° inside the reservoir (the first set of scenarios in Table 1 with varying reservoir Poisson's ratio with ν_r =0.1, 0.2 and 0.3) and the flanks in a compressional and an extensional stress regimes. The higher the reservoir Poisson's ratio (i.e., less compressible reservoir), the lower the κ^{I} (higher tendency to tensile failure). The effect of Poisson's ratio on k^{I} is identical in the two stress regimes. κ^{II} is larger for a reservoir rock with higher Poisson's ratio in the two stress regimes, but the Poisson's ratio effect is more noticeable in an extensional regime.

Fig. 13 shows κ variations as a function of the location of the center of a fault with dip angle of 70° in the caprock (the second set of scenarios in Table 1 with varying caprock Poisson's ratio and a fixed reservoir Poisson's ratio) in a compressional and an extensional stress regime. κ^{I} is not significantly affected for higher Poisson's ratio of the caprock (0.3, 0.2) but, it doubles for ν_s =0.1 for the faults above the reservoir section. In a compressional regime, κ^{II} is not significantly affected by the variation of the caprock Poisson's ratio. This is the opposite to the Poisson's ratio effect in the reservoir in the first set of scenarios. As for the extensional stress regime, the lowest Poisson's ratio leads to a greater κ^{II} above the reservoir. Figures 12 indicates that a fault with dip angle of 70° in the reservoir has a greater risk of mode I and mode II rupture for high Poisson's ratio reservoir rock. In contrast, a 70° fault in the caprock has a greater risk of mode I and mode II rupture for low Poisson's ratio caprock (Figure 13).

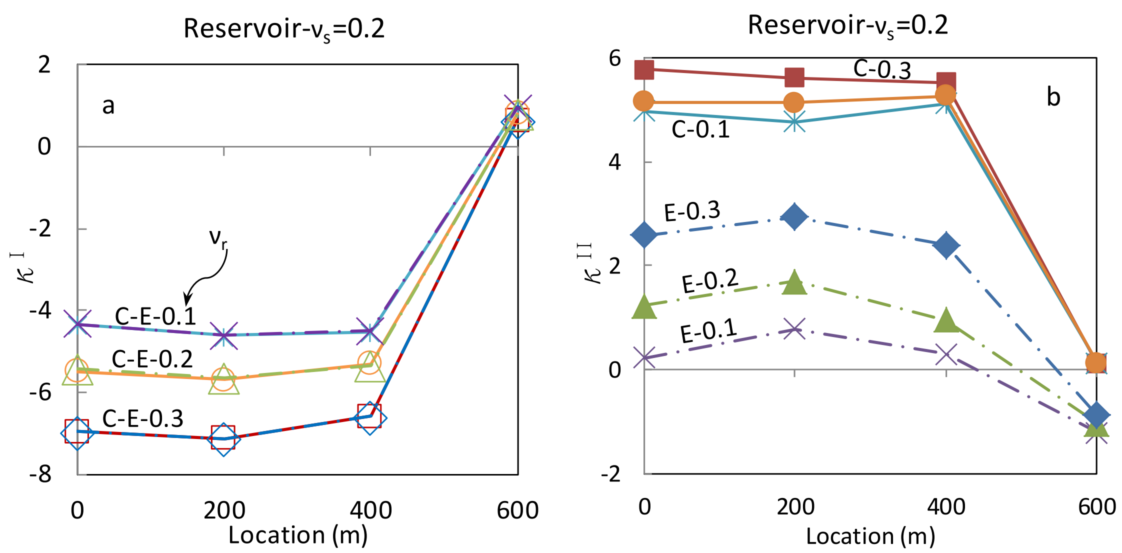

Fig.12 Variation of a) κ^I , b) κ^{II} as a function of the location of the center of a fault with dip angle of 70° in the reservoir and its flank in a compressional (C) and an extensional (E) stress regime for variable Poisson's ratio of the reservoir rock and a fixed value of the caprock Poisson's ratio

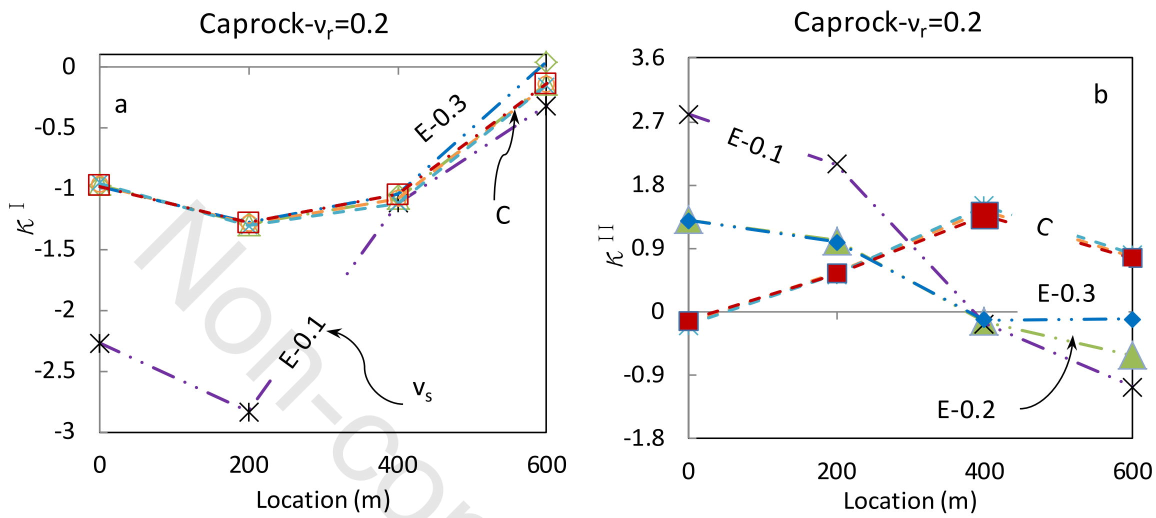

Fig. 13 Variation of a) κ^I , b) κ^{II} as a function of the location of the center of a fault with dip angle of 70° in the caprock in a compressional (C) and an extensional (E) stress regime for variable Poisson's ratio of the caprock and a fixed value of the reservoir Poisson's ratio

Fig. 14 shows κ variations as a function of the location of the center of a fault with dip angle of 70° in the caprock (the third set of scenarios in Table 1 with varying reservoir Poisson's ratio and a fixed caprock Poisson's ratio) for both faults tips in a compressional and an extensional stress regimes. For a lower Poisson's ratio of the reservoir rock, the κ^{II} is greater in the two stress regimes. The greatest changes occur in the caprock above the center and the flanks for an extensional and a compressional stress regime, respectively. Likewise, κ^{I} is lower (greater reduction) for the reservoir rock with low Poisson's ratio. κ^{I} is identical in a compressional and an extensional stress regimes.

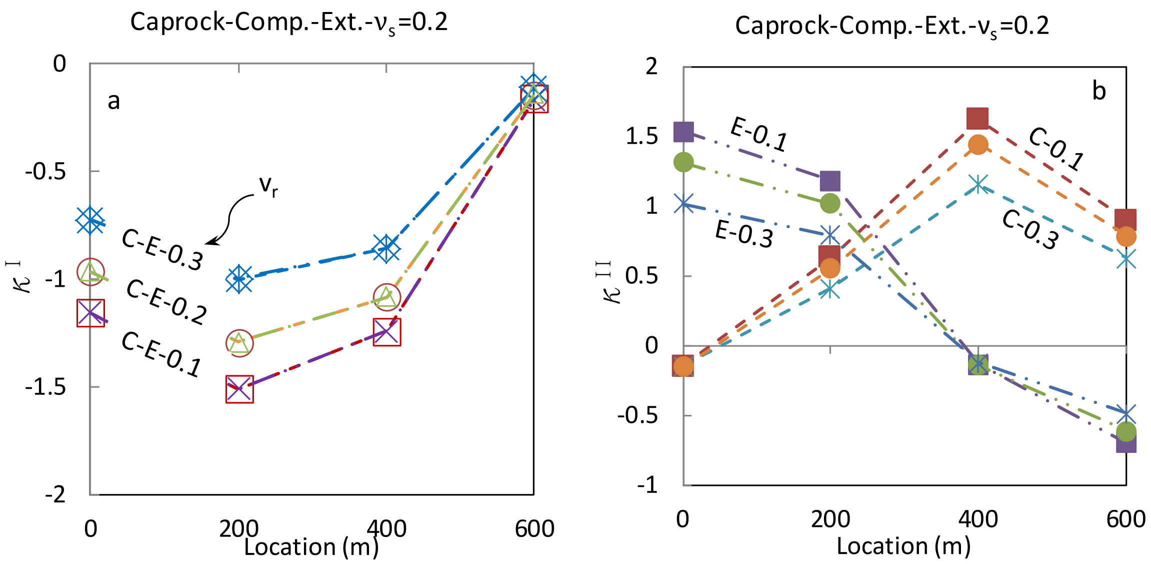

Fig.14 Variation of a) κ^{I} , b) κ^{II} as a function of the location of the center of a fault with dip angle of 70° in the caprock in a compressional (C) and an extensional (E) stress regime for variable Poisson's ratio of the reservoir rock and a fixed value of the caprock Poisson's ratio

3.6. Effect of interaction between faults

Fig. 15 shows variations of κ of a fault with a dip angle of 70° placed at (0,250) in the caprock after reservoir pressurization, where another fault of variable length is present at (200,250), in an extensional and a compressional stress regime. As the length of the adjacent fault increases, there is a greater interaction between the faults, causing the decrease of κ in both modes. This means that a larger fault decreases the rupture risk of a neighboring fault both in mode I and mode II. The reason for this is that the larger fault shields the shorter fault in these examples, where the two faults are parallel in the models. Nevertheless, other fault interaction scenarios may lead to a different result.

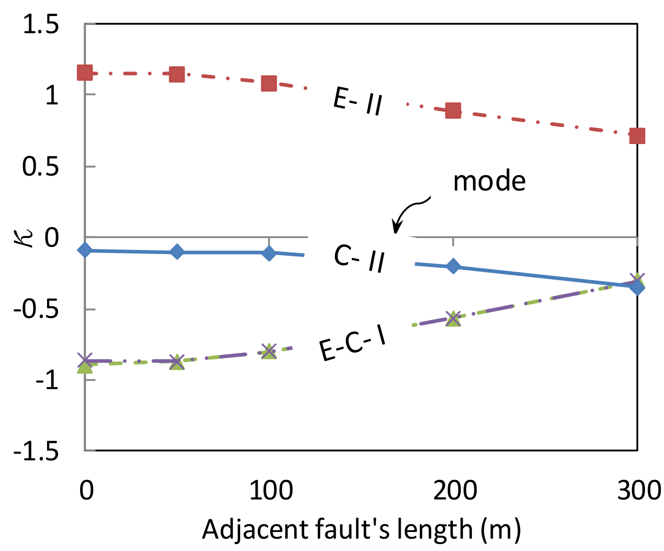

Fig. 15 Variation of κ^{I} and κ^{II} of a fault with dip angle of 70° placed at (0, 250) in the caprock as a function of the length of an adjacent 70° fault placed at (200,250) in an extensional and compressional stress regimes

3.7. Effect of reservoir aspect ratio

Fig. 16a-b show κ variation for a fault with dip angle of 30° in the reservoir and the flank for several reservoir aspect ratios. κ^{I} and κ^{II} are lower and higher for lower aspect ratio reservoirs in a compressional stress regime, respectively. This means that both mode I and mode II rupture likelihood for the fault increases for larger reservoirs in a compressional stress regime. Fig. 16c-d show κ variation for a fault with dip angle of 70° in the caprock in an extensional stress regime. The observed behavior is the opposite of that in the reservoir in a compressional stress regime. Therefore, the risks of rupture growth of the fault decrease for larger reservoirs in an extensional stress regime in the caprock. It is important to note that as the reservoir becomes larger, κ becomes less sensitive to the fault location for a fault with dip angle of 70° and the risks are consequently uniform (Fig. 16c-d). A 30° fault in the reservoir and a 70° fault in the caprock experience the greatest change of SIF in a compressional and an extensional stress regime, respectively.

doi.org/10.1016/j.ijggc.2018.01.004

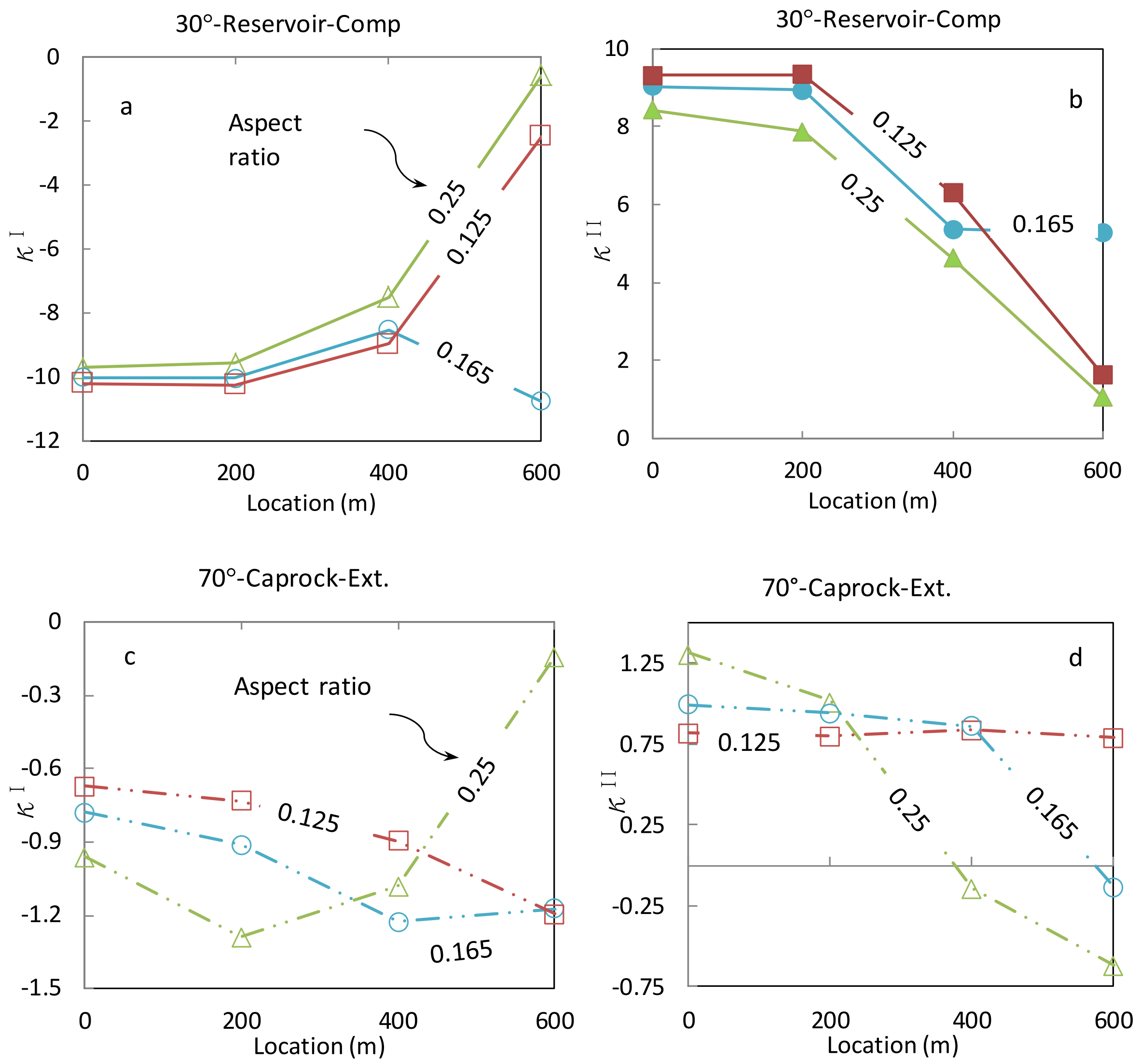

Fig. 16 Variation of a) κ^{I} , b) κ^{II} as a function of the location of a fault with dip angle of 30° in the reservoir in a compressional stress regime and c) k^{I} , d) κ^{II} of fault with dip angle of 70° in the caprock in an extensional stress regime with several reservoir aspect ratio

3.8. Fault rupture analysis

So far, changes of intensity factors have been investigated for mode I and mode II due to injection. However, it is important to obtain the direction and values where the minimum and the maximum SIF occur. First, the critical directions θ^{IC} and θ^{IIC} are calculated (Eqs.(18) and (20)). Then, the minimum K^{I} as K^{Ie} and the maximum K^{II} as K^{IIe} are obtained (Eqs. (19) and (21)). K^{Ie} should always be either negative, meaning tensile opening, or zero, meaning no tensile stress. The type of fault/joint rupture is

doi.org/10.1016/j.ijggc.2018.01.004

distinguished by the criteria in Eqs. (11) and (16). Fig. 17a represents K'^{IIe} and $\left|K^{IIe}/K^{Ie}\right|$ for a 100 m length fault with dip angle of 30° placed at the point (0,0) in the reservoir as a function of several stress ratios (λ), before (ΔP=0) and after injection (ΔP=15 MPa) in an extensional stress regime. K'^{IIe} increases after injection for decreasing λ values until $\lambda = 0.6$, but below this anisotropy ratio, K'^{IIe} remains unchanged. $\left|K^{IIe}/K^{Ie}\right|$ ratio remains constant for all λ and equal to 0.866. The upper dashed line is the ratio of toughness values, i.e., K^{IIC}/K^{IC}, and the lower dashed line is K'^{IIC} (normalized toughness). The toughness values and their ratio are not representing any specific rock type in this study. However, based on some experimental studies in the literature, K^{IIC}/K^{IC} >1 for ambient and reservoir conditions for several rock types (Al-Shayea 2000; Rao et al., 2003; Backers and Stephansson 2012). Based on the criterion in Eq. (16), mode II rupture can occur only if the $\left|K^{IIe}/K^{Ie}\right|$ is above the K^{IIC}/K^{IC} line. Therefore, Figure 17a shows that the mode II rupture of the fault will not occur after injection in the investigated case.

Fig. 17b displays the variation of K'^{Ie} for the same fault as a function of λ as well as the possible direction of mode I rupture before and after reservoir pressurization in an extensional stress regime. Fluid injection decreases K'^{Ie} for λ < 0.6, which increases the risk of mode I rupture. K'^{Ie} remains unchanged and zero for λ > 0.6. $\theta^{IC} = 71°$ is the direction in which tensile failure may occur. Since the minimum principal stress is in the horizontal direction in an extensional stress regime, there is a chance of rupture growth upwards if pressure is kept increasing.

Fig. 17c-d show K'^{IIe}, $\left|K^{IIe}/K^{Ie}\right|$, K'^{Ie} and θ^{IC} for the same fault in a compressional stress regime as a function of λ. The variation of K'^{Ie} and K'^{IIe} have trends similar to the fault in an extensional stress regime in Fig. 17a-b. However, the quantities are greater for the compressional case. Even though the K'^{IIe} value is more than twice in this case, still $\left|K^{IIe}/K^{Ie}\right|$ is 0.866 and lower than 1 and the analysis does not predict a shear rupture. However, the risk of mode I rupture is greater for the compressional case but the minimum principal stress is in the vertical direction in a compressional stress regime. Therefore, the initiated rupture will most likely become horizontal if pore pressure builds up further. Moreover, mode I rupture can occur for larger ranges of λ in a compressional stress regime than in an extensional stress regime.

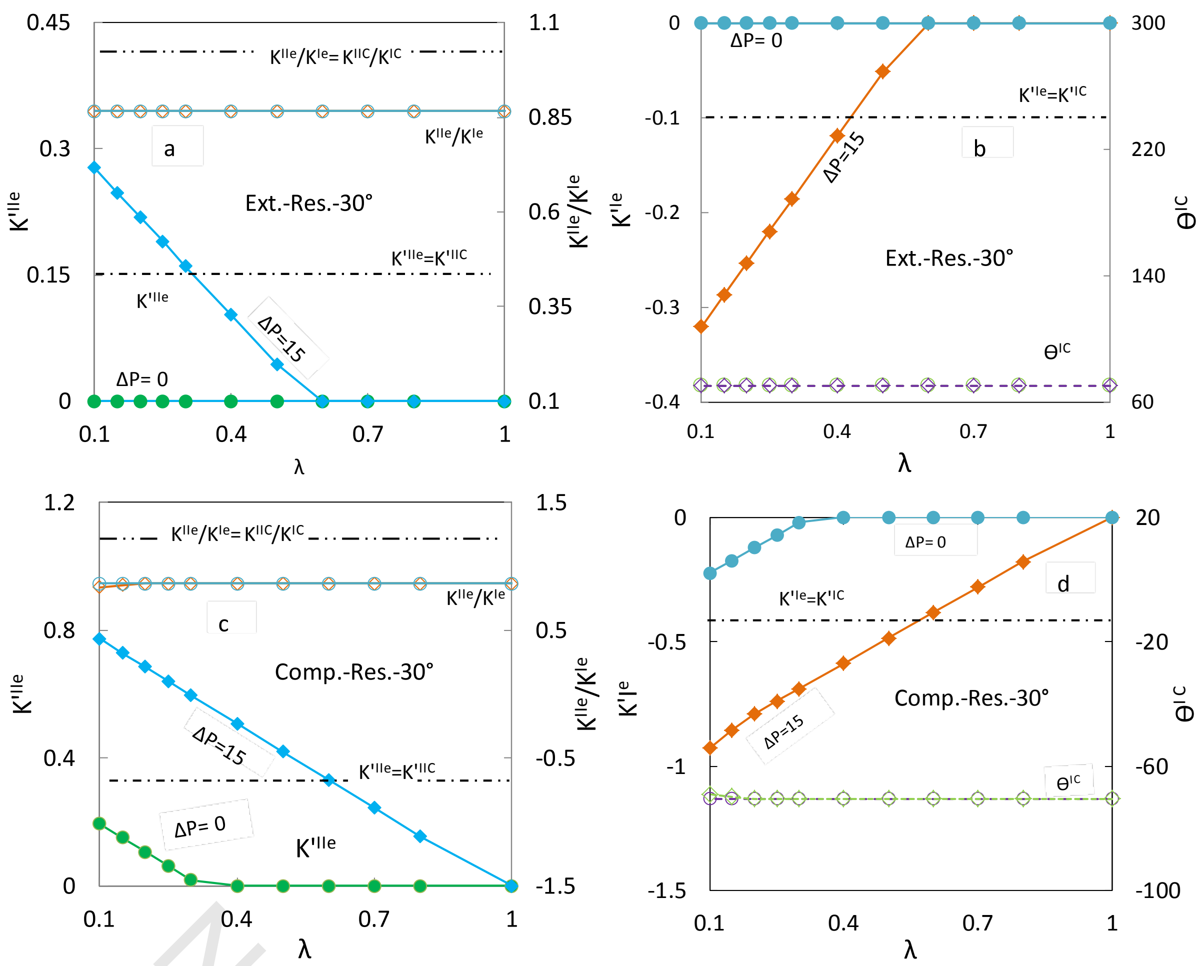

Fig. 17 Variation of the normalized a) K'^{IIe} and b) K'^{Ie} in an extensional and c) K'^{IIe} and d) K'^{Ie} in a compressional stress regime as a function of λ for initial and after 15 MPa pore pressure increase in the reservoir for a fault with dip angle of 30° inside the reservoir. b) and d) also include the probable direction of mode I rupture and the corresponding generic fault rupture criteria

Fig. 18 shows the same features as Fig. 17 for a 100 m length fault with dip angle of 30° placed in the caprock at the point (0,250) as a function of the stress ratio (λ), before (ΔP=0) and after reservoir pressurization (ΔP=15 MPa) in compressional stress regimes. K'^{IIe} and K'^{Ie} decrease (less shear) and increase (less tensile) after injection in a compressional stress regime, respectively, and no mode I and II rupture is possible for the fault in the caprock. Also, the same fault does not experience a change in K'^{IIe} and K'^{Ie} in the caprock in an extensional stress regime and thus, it remains safe.

doi.org/10.1016/j.ijggc.2018.01.004

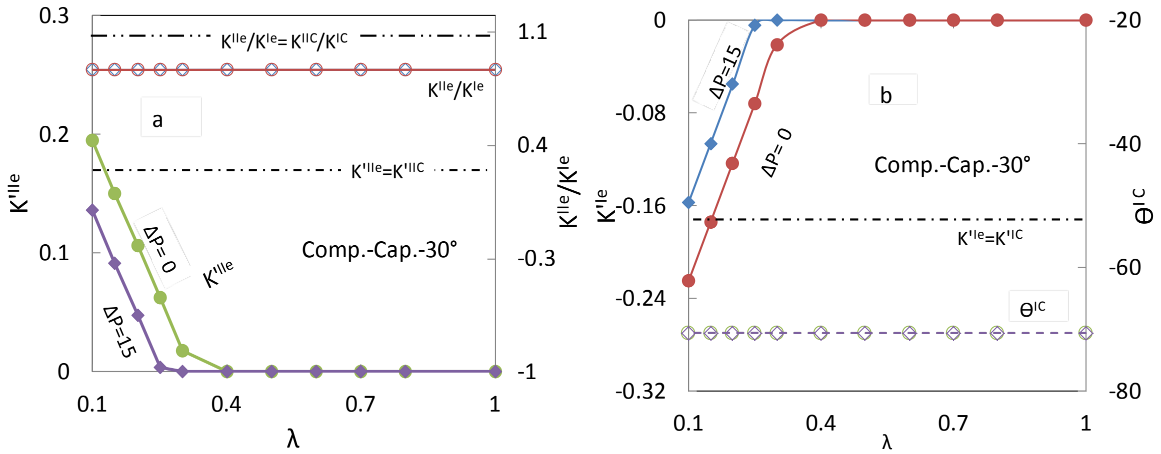

Fig. 18 Variation of the normalized a) K'^{IIe} and b) K'^{Ie} in a compressional stress regime as a function of the stress ratio λ for initial and after 15 MPa pore pressure increase in the reservoir for a fault with dip angle of 30° in the caprock (0,250), a) and b) also include the probable direction of mode I rupture and the corresponding generic fault rupture criteria

Fig. 19 shows the same plots as Fig. 17 for a 100 m length fault with dip angle of 70° placed in the reservoir at (0,0) as a function of the stress ratios (λ), before and after reservoir pressurization in the two stress regimes. Fig. 19a and 19c shows that mode II rupture is not likely for a 70° fault in the reservoir. However, there is a high chance of mode I rupture for λ lower than 0.5 in an extensional stress regime with probable rupture direction of 71° (Fig. 19b). In contrast, mode I rupture is unlikely in a compressional regime (Fig. 19d) because of very low K'^{Ie}. Comparison between Fig. 17b, d and Fig. 19b, d indicates that a 30° fault is more prone to mode I rupture than a 70° fault in the reservoir. Nevertheless, the mode I rupture initiated in front of the 30° fault in a compressional stress regime will rotate to grow horizontally, not only which may not affect caprock integrity but also increase horizontal permeability in the favor of CO_2 storage (Papanastasiou et al., 2016; Vilarrasa and Laloui, 2016). On the other hand, the mode I rupture initiated from the steeper fault in an extensional stress regime would grow upwards, compromising caprock integrity.

doi.org/10.1016/j.ijggc.2018.01.004

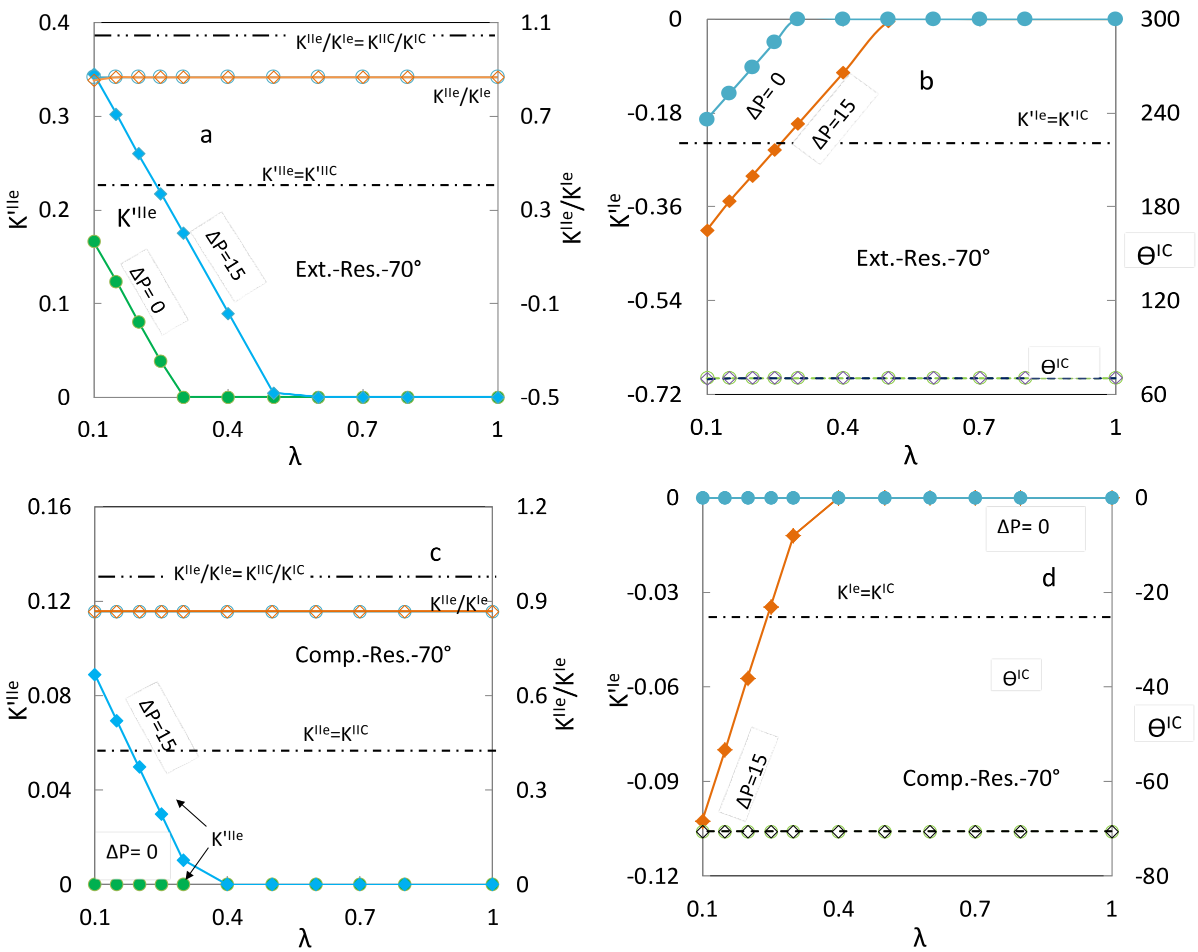

Fig. 19 Variation of the normalized a) K'^{IIe} and b) K'^{Ie} in an extensional and c) K'^{IIe} and d) K'^{Ie} in a compressional stress regime as a function of the stress ratio λ for initial and after 15 MPa pore pressure increase in the reservoir for a fault with dip angle of 70° inside the reservoir, b) and d) also include the probable direction of mode I rupture and the corresponding generic fault rupture criteria

Fig. 20 represents K'^{IIe} and K'^{Ie} for the 70° fault placed in the caprock at (0,250) in an extensional stress regime. The fault is stable in a compressional stress regime in terms of both mode II and mode I ruptures. However, mode I rupture is likely for lower λ in an extensional stress regime.

doi.org/10.1016/j.ijggc.2018.01.004

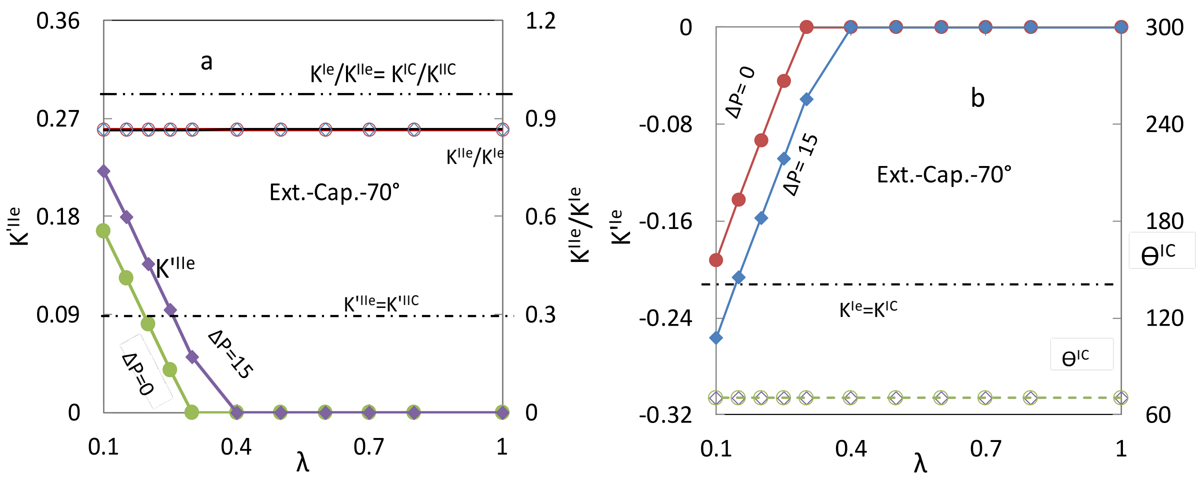

Fig. 20 Variation of the normalized a) K'^{IIe} and b) K'^{Ie} in an extensional stress regime as a function of the stress ratio λ for initial and after 15 MPa pore pressure increase in the reservoir for a fault with dip angle of 70° in the caprock (0,250), a) and b) also include the probable direction of mode I rupture and the corresponding generic fault rupture criteria

4. Discussion

We have developed a methodology that can be used to investigate the rupture growth of faults inside and outside of a reservoir after injection based on LEFM. This methodology can also be applied in reservoir depletion. According to Bazant and Planas (1997), LEFM can be applied to structures with cracks that are small compared to the size of the structure. This may be valid for fractures and faults in geological formations.

Simulation results indicate that κ is directly dependent on the pore pressure increase and consequently, on the stress change induced by that pore pressure increase. An increase of fluid pressure induces a tensile stress in front of the crack/fault tip. The higher the fluid pressure increase, the greater the tension/unloading. But pore pressure change, either due to injection or depletion, induces a poroelastic response that alters the total stresses as well. This alteration of total stresses is not limited to the region which is overpressurized or depleted. Actually, it also propagates a certain distances into the overburden (caprock), the reservoir flanks and in the underburden (basement). This can lead to failure of fractures/faults in locations different than the reservoir, including the caprock.

doi.org/10.1016/j.ijggc.2018.01.004

κ^{I} decreases where the stress component normal to the fault/joint plane decreases or is unloaded. On the other hand, κ^{II} increases if the shear stress applied on the plane increases due to the induced stresses. There is a direct relationship between k^{I} and κ^{II}, if κ^{I} decreases, it means that the shear resistance of the plane decreases, which leads to a higher κ^{II} value.

The results show that κ^{I} is independent of the *in situ* stress regime. This is due to the fact that the stresses induced by poroelastic effects are independent of the stress regime (Gheibi et al., 2016, 2017). Therefore, κ^{I}, as a dependent parameter on the changes in the normal stresses to the faults, is the same in the two stress regimes. Both κ^{I} and κ^{II} are also constant regardless of the minimum to the maximum principal stresses ratio (λ). However, κ^{II} is different for extensional and compressional stress regimes (Tables 2 and 3). Simulation results indicate that it is neither straightforward nor intuitive to predict the rupture likelihood of a fault. It is dependent on the fault inclination, location, size of the over-pressured region, *in situ* stress (both the stress regime and the ratio of the minimum to the maximum stress), fault plane's friction coefficient, elastic properties of the reservoir and caprock and their contrast and mode I and II toughness values of the rock in front of the fault tip. Generally, faults with a high and a low dip angle experience a greater risk in extensional and compressional stress regimes, respectively.

In a compressional stress regime, the hanging wall of a fault tends to move upwards while its footwall tends to move downwards. For a fault bounded inside the reservoir (in its central part), the shear stress increases in compressional stress regime as a result of the increase in the horizontal total stress induced by reservoir pressurization after injection, which leads to an increase in its displacement tendency (Gheibi et al., 2016, 2017). At the same time, κ^{I} decreases due to the reduction in effective stresses. These two effects, i.e., the increase of shear stress and decrease of normal effective stress, increase κ^{II}, which means that the risk of propagation of fault rupture in mode II increases. However, in an extensional stress regime, the hanging wall of a fault tends to move downwards while its footwall tends to move upwards. For the same fault inside the reservoir (in its central part), the shear

doi.org/10.1016/j.ijggc.2018.01.004

stress decreases after injection in an extensional stress regime, leading to a decrease in the tendency. Thus, even though κ^{I} decreases due to the reduction in effective stresses, the increase of κ^{II} is lower in an extensional stress regime than in a compressional one. In other words, κ^{I} is dependent on the change of normal stresses to the fault plane, and the normal stress changes is equal independent of the stress regime. Therefore, κ^{I} is identical for extensional and compressional stress regimes. However, shear stresses acting on a fault plane (inside a reservoir), increases in a compressional stress regime and decreases in an extensional stress regime. Variation of κ^{I} and κ^{II} can be explained based on stress path coefficients (Hettema et al., 2000) and recent paper by Gheibi et al. (2017).

The increase or decrease of the shear or normal effective stresses on a fault plane depend on the location of the fault. Therefore, κ^{II} and κ^{I} vary depending on the fault location. The shear stress increases and decreases in an extensional stress regime in the caprock above the reservoir center and reservoir edge, respectively. It is the opposite in a compressional stress regime. Therefore, while a fault is more likely to propagate in the caprock above the reservoir center in an extensional stress regime, it is more likely to propagate in the reservoir edge in a compressional stress regime.

The fault length has also an effect on fault propagation because the tips of longer faults are more distant from the reservoir. Since, stress changes induced by injection or depletion become lower for longer distances, shorter faults in the central parts and the flank display a greater decrease and increase in κ^{II}, respectively (Fig. 9a).

Toughness is a key parameter in evaluating rupture of a fault. According to the literature, the toughness value is in the range of a few MPa.m$^{0.5}$ in lab-sized samples (Backers and Stephansson 2012; Chang et al. 2002; Ouchterlony 1983). However, the calculated SIF for field-scale faults in their initial state under high stresses is much higher than the toughness obtained in the lab. In spite of the fact that SIF is higher than fracture toughness, most faults are stable. Therefore, investigation of real fault propagation may not be correct using lab scale toughness results and upscaling techniques may be necessary. Husseini et al. (1975) found fracture energy to vary from 1 to 10^{6} J.m$^{0.5}$. This energy is much larger than the Griffith surface energy of minerals estimated by Brace & Walsh (1962) to be 1 to

10 J.m$^{0.5}$. Furthermore, Li (1987) reported energy release rate of earthquakes, g^c, to be 10^6-10^8 J.m$^{0.5}$. Therefore, the corresponding toughness values are much greater than lab results and are relatively in the same order of magnitude of SIF of a fault that we have calculated in this paper. Actually, the relation between intensity factors and the energy release rate is given by (Li, 1986)

$$g = \frac{1-\nu}{2G}\left[\left(K^{I}\right)^2 + \left(K^{II}\right)^2 + \frac{1}{1-\nu}\left(K^{III}\right)^2\right], \tag{38}$$

where G is the shear modulus. Therefore, estimates can be found for K^{IC} and K^{IIC} for a specific g^c value. It is also possible to calculate g for a particular fault with K^{I} and K^{II} (2D) and use rupture criterion $g = g^c$.

Rupture direction of mode I failure shows the initial direction of the rupture. Nevertheless, if the rupture has the possibility to grow, it will grow in the direction perpendicular to the minimum principal stress (Klee et al., 2011). Growth of mode I rupture in confined conditions requires high tensile stress values; therefore, it may stop growing unless high pressurization is maintained. According to Papanastasiou et al. (2016), "in the ductile regime and close to the limit at which a fracture requires high energy to propagate in mode I, there is potential risk for initiation of shear fractures, which may connect with other pre-existing fractures and faults".

Some researchers have reported that experiments performed in rocks can result in propagation of a mode II crack when the compressive load is very high, after the occurrence of a mode I crack (Lajtai, 1974; Petit and Barquins, 1988; Reyes, 1991; Reyes and Einstein, 1991; Shen, 1993; Shen et al., 1995; Bobet and Einstein, 1998; Bobet, 2000; Rao et al., 2003), pure mode II cracks were obtained in experiments under uniaxial or biaxial compressive load. It has been observed that the tensile (mode I) wing cracks start to grow initially and shear cracks (mode II) evolve as secondary cracks. The obtained direction of K'^{IIe} corresponding to the maximum shear stress are also along the fault planes in this study. The results show that mode I rupture has higher chance to be initiated in some of the scenarios presented in the paper, but no mode II rupture is predicted to occur. The reason is that the $\left|K^{IIe}/K^{Ie}\right|$ is always lower than 1 in the studied cases but the K^{IIC}/K^{IC} >1 for ambient and reservoir conditions for several rock types (Al-Shayea 2000; Rao et al., 2003; Backers and Stephansson 2012). However, the existence of the secondary shear crack in the lab-sized experiments is a proof that shear rupture can occur after the mode I ruptures predicted in this study. Therefore, answering to the question whether a rupture can grow upwards requires further investigation. In particular, since formation of the initial mode I rupture changes the local stresses, mode II SIF of the fault/fracture and potential conditions for secondary mode II rupture should be analyzed. Thus, it cannot be confirmed whether mode II rupture is or is not likely after injection in real life for sure at this point using Eqs. (11) and (16) as the rupture criterion

Dependency of toughness of a rock (lab scale) on confining pressure and temperature (Funatsu et al. 2004; Al-Shayea et al. 2000) increases the uncertainty of the occurrence of mode I and mode II propagation. Nevertheless, the reader can analyze the rupture likelihood of the modeled faults for any K^{IC} and K^{IIC} depending on any rock type for a broad *in situ* stress range using the presented results in the paper.

In this study, the friction coefficient was assumed to be constant and equal to 0.6 (Byerlee 1978). However, the friction coefficient may decrease (softening) after slip and reache a residual value in slip-weakening faults which can strongly affect the fault rupture propagation behavior. Stress drop due to slip-weakening is a key driver in rupture of faults (Li, 1986). It is important to note that two types of stress drop can occur in a fault. Stress drop can be due to pore pressure and total stress changes and to slip-weakening. The later one is lacking in this study and further investigation is required for more reliable results. However, as an example, Fig. 21 represents K'^{IIe} and $\left|K^{IIe}/K^{Ie}\right|$ for faults with dip angle of 70° that have different residual friction coefficient (i.e., shear stress drop) and are placed in the caprock at (0,250) in an extensional stress regimes. It is clear that K'^{IIe} becomes greater for the lower residual friction coefficient, presenting a greater risk for the fault rupture growth.

doi.org/10.1016/j.ijggc.2018.01.004

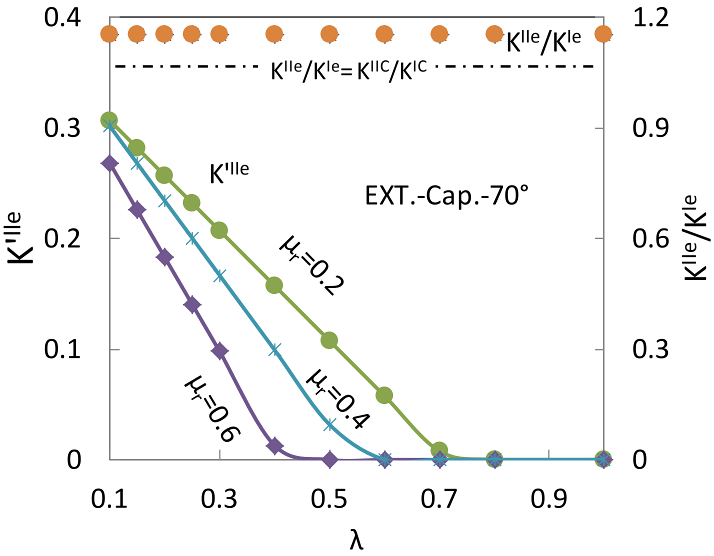

Fig. 21 Variation of the normalized K'^{IIe} as a function of the stress ratio λ for initial and after 15 MPa pore pressure increase in the reservoir for a fault with dip angle of 70° placed in the caprock at (0,250), for several residual friction coefficient (μ_r) in an extensional regime

In this study, the focus is on simple reservoir-caprock geometries. However, the reservoir geometry, such as inclination, affects the stress changes (Soltanzadeh et al., 2008). In the field, it is often observed that several faults cut the reservoir-caprock and several compartments of the reservoir are available that can be used as storage sites. The results indicate that the interaction of faults, affect the calculated stress intensity path (Section 3.6). Therefore, detailed studies of each injection sites should be performed including all the available geological information into the models.

The model used in the paper is 2D plane-strain. In a 3D system, if the fault strike is perpendicular to the X-Y plane shown in Fig. 5, the results (stress intensity paths) can be directly used in the rupture analyses. However, the stress redistribution is a spatial variable and faults crossing the same point and presenting the same properties, but having different strike direction, will have different stress intensity path. Besides, in a 3D system, the mode III failure mode should also be taken into account and κ^{III} should be defined and measured for faults following the same methodology.

Fluids, like CO_2, which are injected in deep geological formations, generally reach the storage formation at a lower temperature than that of rock (Vilarrasa and Rutqvist 2017). This temperature drop induces thermal stresses that may affect the initial and secondary intensity factors after injection.

Thermal effect induce tension, which decrease the K^{I} and changes K^{II}. This may lead to a change in fault stability and its rupture likelihood. Moreover, chemical reactions of the rock and injected fluid may lead to decrease of rock fracture toughness (Anderson and Grew 1977). These couplings may be an important issue in the long-term stability of faults and fractures.

In our analyses, it is assumed that pressure buildup is not diffused into the caprock and the section of faults in the caprock. However, diffusion of pressure into caprock may have short-term and long-term consequences due to providing a driving force in the fault tip as well as decreasing the effective stresses, leading to a less compressive condition. Also, the undrained effect of caprock was neglected. Deformation of the caprock due to the inflation of the reservoir after injection will change the pore pressure in the caprock proportionally to the Skempton coefficient, which is caused by the undrained response of the caprock in the short-term (Fjær et al. 2008; Holt et al. 2017).

The hydro-mechanical full coupling would provide a more realistic pore pressure distribution in the reservoir and the caprock and consequently more precise stress changes, therefore, a more realistic κ^{I} and κ^{II}. However, this only affects the quantities and the methodology can be extended for any flow simulation and flow boundary conditions. Also, including fluid flow in the fractures/faults. could capture important features in fault rupture propagation.

The developed methodology (not results) is independent of thermo-hydro-mechanical couplings, flow of fluid in the fault/fracture and diffusion of the pressure into the caprock. The reason for this non-dependency is that the methodology only uses the internal forces of the contacts of clusters to calculate K and consequently κ. Thus, the aspects that are currently lacking in our model, such as thermoelasticity, geochemistry or pressure diffusion into the caprock, can be incorporated in the solution calculated in MDEM, which will calculate the internal forces, from which the rupture analyses can be done afterwards.

5. Conclusion

A methodology has been developed to study mode I and mode II rupture of faults/fractures inside the reservoir and the caprock due to reservoir pressurization. The proposed methodology has the capability to obtain the direction of mode I and mode II rupture in front of a fault/fracture tip based on the minimum tensile and the maximum shear stress directions. The methodology follows the assumptions of LEFM and was embedded into a hybrid FEM-DEM in-house code called MDEM.

Two new coefficients have been defined as stress intensity path (κ) for a fault/fracture. These coefficients are similar to stress path and are defined as the change of SIF of a given fault/fracture per unit pore pressure change of the reservoir after injection for mode I and mode II failures. Additionally, some relationships (Eqs. (18)-(21)) were proposed to calculate the critical overpressure that should not be exceeded to avoid the propagation of the two modes that can be used for given faults with known κ.

Stress intensity path depends on stress regime, location, dip angle and length of faults, Poisson's ratio of the reservoir and caprock as well as the reservoir aspect ratio. Generally, κ is greater for faults inside the reservoir and in the caprock for compressional and an extensional stress regimes, respectively. Longer faults have higher mode I (less tensile opening) and higher mode II (greater shear) κ. Faults in the caprock become more stable as the reservoir is larger (lower aspect ratio), but the rupture likelihood increases for faults inside a reservoir at the same time.

Simulation results indicate that mode I failure is likely for faults with low dip angle inside the reservoir for compressional stress regimes. However, the initiated mode I failure may not have the chance to grow upwards in a compressional stress regime, because the minimum principal is in the vertical direction. Therefore, the initiated rupture may rotate to grow horizontally to increase the horizontal permeability of the reservoir. In contrast, mode I rupture is likely for faults with high dip angle in the caprock in extensional stress regime. The initiated rupture in this case, may grow upwards if pore pressure is maintained or increased. Results indicated that mode II rupture is not likely in any of the investigated scenarios with the assumption K^{IIC}/K^{IC} >1.

doi.org/10.1016/j.ijggc.2018.01.004

Acknowledgements

This publication has been produced with partial support from the BIGCCS Centre, performed under the Norwegian research program Centres for Environment-friendly Energy Research (FME). The first two authors acknowledge the following partners for their contributions: Gassco, Shell, Statoil, TOTAL, ENGIE, and the Research Council of Norway (193816/S60). V.V. acknowledges financial support from the “TRUST" project (European Community's Seventh Framework Programme FP7/2007-2013 under grant agreement no. 309607) and from “FracRisk" project (European Community's Horizon 2020 Framework Programme H2020-EU.3.3.2.3 under grant agreement no. 636811). Authors are also grateful to SINTEF Petroleum Research providing the MDEM code.

References

Alassi HT (2008) Modeling reservoir geomechanics using discrete element method: Application to reservoir monitoring PhD thesis at NTNU Trondheim Norway

Al-Shayea NA, Khan K, Abduljauwad SN (2000) Effects of confining pressure and temperature on mixed-mode (I–II) fracture toughness of a limestone rock International Journal of Rock Mechanics and Mining Sciences 37:629-643 doi:http://dx.doi.org/10.1016/S1365-1609(00)00003-4

Anderson OL, Grew PC (1977) Stress corrosion theory of crack propagation with applications to geophysics Reviews of Geophysics 15:77-104 doi:10.1029/RG015i001p00077

Backers T, Stephansson O (2012) ISRM Suggested Method for the Determination of Mode II Fracture Toughness Rock Mechanics and Rock Engineering 45:1011-1022 doi:10.1007/s00603-012-0271-9

Bažant ZP, Oh BH (1983) Crack band theory for fracture of concrete Matériaux et Construction 16:155-177 doi:10.1007/bf02486267

Bazant ZP, Planas J (1997) Fracture and size effect in concrete and other quasibrittle materials. CRC press,

Bobet A (2000).The initiation of secondary cracks in compression. Engineering Fracture Mechanics 66, 187-219

Bobet A, Einstein H H (1998) Fracture coalescence in rock-type materials under uniaxial and biaxial compression. International Journal of Rock Mechanics and Mining Sciences 35, 863-888.

Byerlee J (1978) Friction of rocks PAGEOPH 116:615-626 doi:10.1007/BF00876528

Cappa F, Rutqvist J (2011) Impact of CO_2 geological sequestration on the nucleation of seismic fault ruptures Am Rock Mechanics Assoc 11

Chang S-H, Lee C-I, Jeon S (2002) Measurement of rock fracture toughness under modes I and II and mixed-mode conditions by using disc-type specimens Engineering Geology 66:79-97 doi:https://doi.org/10.1016/S0013-7952(02)00033-9

Comerlati A, Ferronato M, Gambolati G, Putti M, Teatini P (2006) Fluid-dynamic and geomechanical effects of CO_2 sequestration below the Venice Lagoon Environmental & Engineering Geoscience 12:211-226

Cundall PA, Strack ODL (1979) A discrete numerical model for granular assemblies Géotechnique 29:47-65 doi:10.1680/geot.1979.29.1.47

de Morais AB (2007) Calculation of stress intensity factors by the force method Engineering Fracture Mechanics 74:739-750 doi:http://dx.doi.org/10.1016/j.engfracmech.2006.06.017

Erdogan F, Sih GC (1963) On the Crack Extension in Plates Under Plane Loading and Transverse Shear Journal of Basic Engineering 85:519-525 doi:10.1115/1.3656897

Fjar E, Holt RM, Raaen A, Risnes R, Horsrud P (2008) Petroleum related rock mechanics vol 53. Elsevier, Amsterdam

Funatsu T, Seto M, Shimada H, Matsui K, Kuruppu M (2004) Combined effects of increasing temperature and confining pressure on the fracture toughness of clay bearing rocks International Journal of Rock Mechanics and Mining Sciences 41:927-938 doi:http://doi.org/10.1016/j.ijrmms.2004.02.008

Gheibi S, Holt R, Vilarrasa V Stress path evolution during fluid injection into geological formations. In: 50th US Rock Mechanics/Geomechanics Symposium, 2016. American Rock Mechanics Association,

Gheibi S, Holt RM, Vilarrasa V (2017) Effect of faults on stress path evolution during reservoir pressurization International Journal of Greenhouse Gas Control 63:412-430 doi:https://doi.org/10.1016/j.ijggc.2017.06.008

Hansen, O., Gilding, D., Nazarian, B., Osdal, B., Ringrose, P., Kristoffersen, J. B., ... & Hansen, H. (2013). Snøhvit: the history of injecting and storing 1 Mt CO_2 in the Fluvial Tubåen Fm. *Energy Procedia*, *37*, 3565-3573.

Hettema M, Schutjens P, Verboom B, Gussinklo H (2000) Production-induced compaction of a sandstone reservoir: the strong influence of stress path SPE Reservoir Evaluation & Engineering 3:342-347

Holt R, Bauer A, Bakk A (2017) Overburden pore-pressure changes and their influence on 4D seismic. SEG Technical Program Expanded Abstracts 2017: pp. 3632-3636 (https://doi.org/10.1190/segam2017-17727948.1)

Husseini MI, Jovanovich DB, Randall MJ, Freund LB (1975) The Fracture Energy of Earthquakes Geophysical Journal International 43:367-385 doi:10.1111/j.1365-246X.1975.tb00640.x

Itasca (2012) PFC 2D (Particle flow code in 2 dimensions).

Klee, G., Bunger, A., Meyer, G., Rummel, F., & Shen, B. (2011). In situ stresses in borehole Blanche-1/South Australia derived from breakouts, core discing and hydraulic fracturing to 2 km depth. *Rock mechanics and rock engineering*, *44*(5), 531-540.

Lavrov A, Larsen I, Bauer A (2016) Numerical Modelling of Extended Leak-Off Test with a Pre-Existing Fracture Rock Mechanics and Rock Engineering 49:1359-1368 doi:10.1007/s00603-015-0807-x

Lawn BR (1975) Fracture of brittle solids / B. R. Lawn, T. R. Wilshaw. Cambridge solid state science series, vol Accessed from https://nla.gov.au/nla.cat-vn2125360. Cambridge University Press, Cambridge [Eng.] ; New York

Li VC (1986) Mechanics of shear rupture applied to earthquake zones [microform] / by Victor C. Li. NASA contractor report; NASA CR-180070, vol Accessed from http://nla.gov.au/nla.cat-vn4110192. National Aeronautics and Space Administration; National Technical Information Service, distributor, Washington, DC : Springfield

Mas Ivars D, Potyondy DO, Pierce M, Cundall PA (2008) The smooth-joint contact model Proceedings of WCCM8-ECCOMAS 2008:8th

Ouchterlony F (1983) Fracture Toughness Testing of Rock. In: Rossmanith HP (ed) Rock Fracture Mechanics. Springer Vienna, Vienna, pp 69-150. doi:10.1007/978-3-7091-2750-6_3

Papanastasiou P, Papamichos E, Atkinson C (2016) On the risk of hydraulic fracturing in CO_2 geological storage International Journal for Numerical and Analytical Methods in Geomechanics 40:1472-1484 doi:10.1002/nag.2502

Petit J-P, Barquins M (1988) Can natural faults propagate under Mode II conditions? Tectonics 7:1243-1256 doi:10.1029/TC007i006p01243

Rao Q, Sun Z, Stephansson O, Li C, Stillborg B (2003) Shear fracture (Mode II) of brittle rock International Journal of Rock Mechanics and Mining Sciences 40:355-375 doi:http://dx.doi.org/10.1016/S1365-1609(03)00003-0

Reyes O (1991)Experimental study and analytical modelling of compressive fracture in brittle materials. Ph.D. thesis. Massachusettes Institute of Technology, MA, USA

Reyes O, Einstein H H (1991) Failure mechanisms of fractured rock—a fracture coalescence model In: Wittke W. (Ed.) Proceedings of the International Congress on Rock Mechanics Aachen Germany pp. 333–340

Rinaldi, A. P., Rutqvist, J., & Cappa, F. (2014). Geomechanical effects on CO_2 leakage through fault zones during large-scale underground injection. *International Journal of Greenhouse Gas Control*, *20*, 117-131.

Rinaldi AP, Vilarrasa V, Rutqvist J, Cappa F (2015) Fault reactivation during CO_2 sequestration: Effects of well orientation on seismicity and leakage Greenhouse Gases: Science and Technology:n/a-n/a doi:10.1002/ghg.1511

Rutqvist J (2012) The Geomechanics of CO_2 Storage in Deep Sedimentary Formations Geotechnical and Geological Engineering 30:525-551 doi:10.1007/s10706-011-9491-0

Rutqvist J et al. (2016) Fault activation and induced seismicity in geological carbon storage–Lessons learned from recent modeling studies Journal of Rock Mechanics and Geotechnical Engineering 8:789-804

Shen B (1993) Mechanics of fractures and intervening bridges in hard rocks. Ph.D. Thesis. Royal Institute of Technology Stockholm Sweden

Shen B, Stephansson O, Einstein HH, Ghahreman B (1995) Coalescence of fractures under shear stresses in experiments Journal of Geophysical Research: Solid Earth 100:5975-5990 doi:10.1029/95JB00040

Soltanzadeh H, Hawkes CD (2008) Semi-analytical models for stress change and fault reactivation induced by reservoir production and injection Journal of Petroleum Science and Engineering 60:71-85 doi:http://dx.doi.org/10.1016/j.petrol.2007.05.006

Streit JE, Hillis RR (2004) Estimating fault stability and sustainable fluid pressures for underground storage of CO_2 in porous rock Energy 29:1445-1456 doi:http://dx.doi.org/10.1016/j.energy.2004.03.078

Vasco D et al. (2010) Satellite-based measurements of surface deformation reveal fluid flow associated with the geological storage of carbon dioxide Geophysical Research Letters 37

Vidal-Gilbert S, Nauroy J-F, Brosse E (2009) 3D geomechanical modelling for CO_2 geologic storage in the Dogger carbonates of the Paris Basin International Journal of Greenhouse Gas Control 3:288-299 doi:http://dx.doi.org/10.1016/j.ijggc.2008.10.004

Vilarrasa V, Carrera J (2015) Geologic carbon storage is unlikely to trigger large earthquakes and reactivate faults through which CO_2 could leak Proceedings of the National Academy of Sciences 112:5938-5943 doi:10.1073/pnas.1413284112

Vilarrasa V, Laloui L (2016) Impacts of Thermally Induced Stresses on Fracture Stability During Geological Storage of CO_2 Energy Procedia 86:411-419 doi:http://dx.doi.org/10.1016/j.egypro.2016.01.042

Vilarrasa V, Makhnenko R, Gheibi S (2016) Geomechanical analysis of the influence of CO_2 injection location on fault stability Journal of Rock Mechanics and Geotechnical Engineering 8:805-818

Vilarrasa V, Rutqvist J (2017) Thermal effects on geologic carbon storage Earth-Science Reviews 165:245-256 doi:https://doi.org/10.1016/j.earscirev.2016.12.011

Wang L, Bai B, Li X, Liu M, Wu H, Hu S (2016) An Analytical Model for Assessing Stability of Pre-Existing Faults in Caprock Caused by Fluid Injection and Extraction in a Reservoir Rock Mechanics and Rock Engineering 49:2845-2863 doi:10.1007/s00603-016-0933-0

White JA, Foxall W (2016) Assessing induced seismicity risk at CO_2 storage projects: Recent progress and remaining challenges International Journal of Greenhouse Gas Control 49:413-424

Wu LZ, Li B, Huang RQ, Wang QZ (2016) Study on Mode I–II hybrid fracture criteria for the stability analysis of sliding overhanging rock Engineering Geology 209:187-195 doi:http://dx.doi.org/10.1016/j.enggeo.2016.04.022

Zhou J, Yang X, Xing H (2013) Analytical solutions for crack initiation angle of mixed mode crack in solid material Mechanics 19:498-505